Crustal Structure in a Mesozoic Extensional Terrane: The South Georgia Rift and the Epicentral Area of the 1886 Charleston, South Carolina, Earthquake

Jesse Conard Buckner

Thesis submitted to the faculty of the Virginia Polytechnic Institute and State University in partial fulfillment of the requirements for the degree of

Master of Science
In
Geosciences

Martin C. Chapman (Chair)
John A. Hole
J.F. Read

28 January, 2011
Blacksburg, VA

Keywords: Earthquake, Reflection Seismology, South Carolina, Charleston, Refraction Seismology

Crustal Structure in a Mesozoic Extensional Terrane: The South Georgia Rift and the Epicentral Area of the 1886 Charleston, South Carolina, Earthquake

Jesse Conard Buckner

ABSTRACT

On August 31, 1886 a large scale earthquake occurred in Summerville, S.C. causing severe damage in the coastal city of Charleston. Although intensive geological and geophysical studies have been conducted in the area, uncertainty remains about the details of the event. Recently evidence from seismic reflection profiles have shed light on the tectonic environment of the area. The epicentral area of the 1886 event lies within the South Georgia Rift, a Mesozoic rift terrane. Previous studies have revealed clues to the geologic structure and evolution of this feature. SEISDATA4 is the largest seismic reflection profile recorded in the area. By re-processing the line, information about the tectonic structure of the area was revealed. The early Mesozoic extensional basin that hosted the 1886 earthquake and is host to the modern seismicity recorded in the area, extends several kilometers to the south and west of Charleston, along SEISDATA4. Cenozoic and Mesozoic faults were resolved within the basin and along its northwestern boundary that is distinguished by a strong gradient in the magnetic field. However, the question as to which fault was responsible for the rupture of 1886 still remains.

The refraction analysis provides better resolution of the lithology in Lower Mesozoic section. The termination of the strong reflection at the base of the Atlantic Coastal Plain occurs in a section of the profile that shows major disruption of the underlying reflections, and suggests that the termination of a lower Mesozoic basalt flow responsible for the reflection may be related to tectonic deformation.

Acknowledgments

I would like to everyone who has provided me support, motivation, and guidance through this entire process. I would like to graciously acknowledge the many efforts of Martin Chapman to help me through this endeavor. Not only has he been an exceptional teacher, he has also been a great mentor and friend. He has sacrificed many an hour in order to provide not only help, but great conversation and friendship. Also I would like to thank Jake Beale for dedicating the last two years of his life to educating me both in reflection seismology and the ways of the world. Because of his loyalty I will always hold a special place in my heart for the Edmonton Oilers. It's been a privilege to not only work with the two of you, but to also call you my friends.

I would also like to thank all of the friends I've come to know along the way including, but not limited to my fellow Geophysicists in 1070. Keep on keeping on.

My loving Mom and Dad deserve a similar thanks for their dedication to this process, and their willingness to provide me with both the support and motivation to succeed. Love you guys.

Last but not least all the people that made this research possible; Geophyisical Pursuit Inc., Richard Godbee, Miles Gentry, John Hole, Fred Read, the fine folks at Landmark Software, the rest of the Geoscience faculty, and the always helpful staff (especially Connie Lowe).

Table of Contents

List of Figures

Chapter 1: Introduction

A major earthquake occurred on August 31, 1886, causing severe damage to the city of Charleston, South Carolina (Dutton, 1889). Recent magnitude estimates for this earthquake range from 6.9 (Bakun and Hopper, 2004) to M 7.3 (Johnston, 1996). The epicenter of the "Charleston" earthquake was approximately 25 km to the northwest of Charleston, near the village of Summerville (Dutton, 1889). Geological investigations have found evidence for several prehistoric liquefaction-producing earthquakes in coastal South Carolina in the past 6,000 years (summarized in Talwani and Schaeffer, 2001). Consequently, the epicentral area of the 1886 shock has the highest estimated seismic hazard along the east coast of the United States (Petersen et al., 2008). The Charleston earthquake was one of the best-documented shocks of the 19th century and the epicentral area was the site of intensive geological and geophysical investigation in the period 1973-1983 (Rankin, 1977; Gohn, 1983a). However, much uncertainty remains concerning the tectonic origin of the seismicity and associated seismic hazard.

The goal of the research described here is to further resolve the geological structure of the shallow crust in the epicentral area of the 1886 earthquake, hopefully leading to a better understanding of the tectonic process responsible. The work involved the reprocessing of seismic reflection profile SEISDATA4, an industry line that is the longest of the seismic reflection profiles collected in the area. The line extends from just west of the Charleston peninsula on the South Carolina coast, to near Greenville, in the Piedmont province of northwestern South Carolina. The line exhibits good data at several locations. It was recorded with offsets of up to 4000 meters, which is conducive for looking deep into the recently imaged extensional basin structure and perhaps imaging its base. The objective of the reprocessing of SEISDATA4 is two fold; further imaging of Cenozoic faults associated with reactivation of early Mesozoic faults in

the study area containing the epicenter of the 1886 earthquake, and imaging the structure and limits of the early Mesozoic extensional rift basin that hosted the earthquake.

1.1 Regional Geology

The Charleston-Summerville, South Carolina area lies within a major early Mesozoic extensional terrane known as the South Georgia Rift, shown in Figure1.1. The South Georgia Rift (SGR) lies buried beneath Atlantic Coastal Plain sediments in parts of South Carolina, Georgia, Florida, Alabama, and extends into the northeastern portion of the Gulf of Mexico. The SGR is known from well data, potential field interpretation, and seismic reflection profiles (Daniels et al., 1983, Chowns and Williams 1983, Thomas et al., 1989, McBride 1991). A rift lithology consisting of lower Mesozoic basalt-flows, possible diabase intrusions, and clastic sedimentary rocks has been sampled by drilling in a few locations in Georgia and South Carolina. This lithology distinguishes the SGR from the metamorphosed Paleozoic rocks of the Appalachian Piedmont province to the north, and from the Paleozoic felsic rocks of the "Suwannee" terrane of Florida (McBride 1991, Thomas et al. 1989).

The characteristic lithology of the South Georgia Rift is known to exist in the area of the 1886 earthquake epicenter from cores collected at the Clubhouse Crossroads site approximately 25 km to the southwest of Summerville. No drilling has penetrated the entire thickness of the Mesozoic section in the South Carolina portion of the South Georgia Rift. The deepest well in the area (located 70 km to the west of Summerville) penetrated to a depth of 3.8 km and bottomed in basalt or diabase (Talwani, unpublished report, 2000). The actual thickness of the Mesozoic rocks comprising the South Georgia Rift in the study area remains unknown, although Luetgert et al. (1994) interpreted the base of the Mesozoic at 7 km depth on the basis of wide-angle reflection and refraction data.

1.2 Previous Work Using Seismic Reflection Profile Data in the Study Area

Recent discoveries are beginning to shed some light on the geological source of the 1886 earthquake. Reprocessing of seismic reflection profile data collected during the period 1975-1983 has imaged previously unrecognized Mesozoic-Cenozoic faults in the epicentral area (Chapman and Beale 2008, 2010). Figure 1.2 shows a regional total intensity magnetic anomaly map of the study area, the locations of wells that have penetrated through coastal plain sediments into the underlying early Mesozoic section of rift-related rocks, and the locations of seismic reflection profiles reprocessed and interpreted by Chapman and Beale (2008, 2010). This work indentified an extensive early Mesozoic extensional basin lying between Summerville and Charleston. Figure 1.3 shows a CMP stacked section of a part of SEISDATA4 extending from the southeastern end of the profile (CMP 1) to CMP 1400, which is the location of the right-angle bend in the line near the Edisto River. This part of SEISDATA4 is co-located with profile SC4, shown in Figure 1.2 (See also location map, Figure 2.1). Figure 1.3 compares this section with the COCORP 2 (C2) line collected along the south side of the Ashley River, approximately 17 km to the northeast. The similarity of the two profiles is striking, and both show a major syncline-like structure involving the early Mesozoic volcanic and sedimentary rocks beneath the coastal plain sediments. The tectonic significance of this feature was initially recognized by Chapman and Beale (2010) and has been interpreted as an extensional basin defining a zone of intense continental rifting within the larger South Georgia Rift. One of the objectives of this study is to determine whether or not Cenozoic-Mesozoic faults similar to those imaged and described by Chapman and Beale (2008, 2010) that are located nearer Summerville also exist to the south along SEISDATA4. This has important implications for seismic hazard in the study area and broader region.

Figure 1.4 shows the previously interpreted geometry of the extensional basin in plane view. The northwestern boundary of the basin is marked by a magnetic gradient that passes through the northwestern section of the town of Summerville and is spatially correlated with seismicity (Figures 1.2 and 1.4). Folding of Cretaceous and Tertiary sediments, fault–edge diffractions and truncation and offset of the basement reflections has been observed at all four locations where seismic reflection profiles cross the magnetic gradient (indicated by F2-F5 in Figure 1.4). This indicates that the northwestern boundary of this basin is controlled by faulting (Chapman and Beale 2010). There is also evidence for Cenozoic faulting within the interior of the basin, on profile VT3, at the location indicated by F1 in Figure 1.4, which coincides with the epicenters of the most active cluster of earthquakes located in the study area.

The best imaged and perhaps the most significant fault recognized to date in the study area is observed on profile VT3 (Figure 1.5). The "B" reflector on profile VT3 shows a large down-to-the-southeast offset. The reflector is offset by approximately 200 meters (Chapman and Beale 2008). The fault was originally referred to as fault C by Chapman and Beale (2008). The location is indicated by the circle and F1 label in Figure 1.4. Along with obvious offset in the Lower Mesozoic volcanic and sedimentary rocks, fault C truncates and offsets the overlying Late Cretaceous and Tertiary sediments of the Coastal Plain. The coastal plain sediments show up-to-the-southeast offset; interpreted as evidence for compressional reactivation of the Lower Mesozoic extensional faulting by Chapman and Beale (2008, 2010).

The most prominently imaged horizon in the area is the "J" reflector, a basalt flow radiogenically dated to the early Jurassic, and known to uncomformably underlie coastal plain sediments of Late Cretaceous age from cores collected at the Clubhouse Crossroads boreholes (Gohn, 1983a and 1983b). The J reflection is important because it is associated with what is

referred to in the following as the “post-rift unconformity" (PRU) marking the hiatus between eruption and deposition of volcanic rocks and clastic sediments associated with active Lower Mesozoic continental rifting and initial opening of the Atlantic, and deposition of Late Cretaceous-Cenozoic sediments of the developing Atlantic passive margin. The VT3 profile shows that the basalt responsible for the J reflection is much younger than the underlying B units. Although the direction of offset of the J basalts by fault C on VT3 is the same as the older B units (down-to-the-southeast) there is much less deformation, on the J, indicating that most of the Lower Mesozoic extensional faulting along the VT3 profile took place before the eruption of the J basalt.

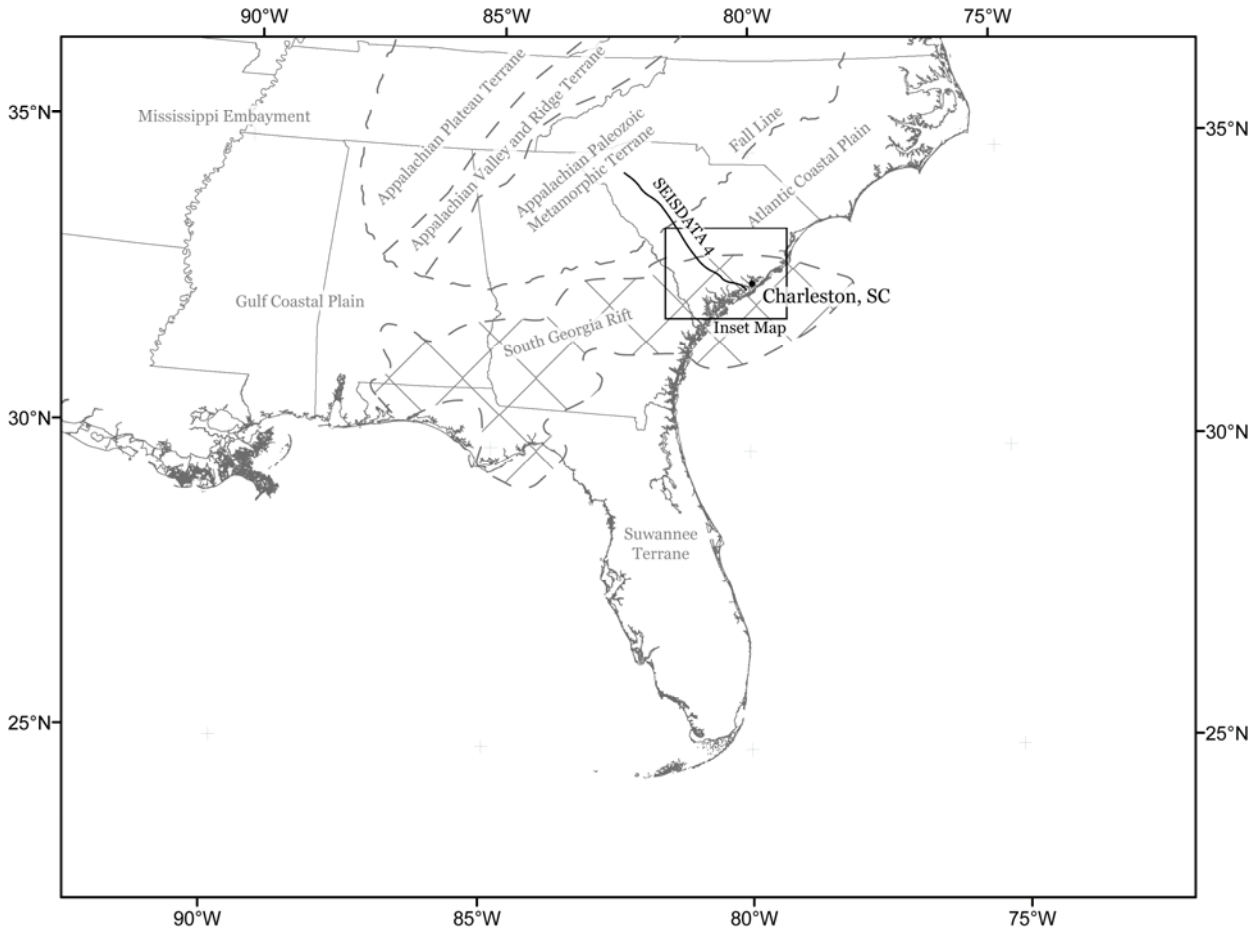

Figure 1.1: Map showing exposed geological provinces in the southeastern United States. The buried, rifted terrane known as the South Georgia Rift and the buried Suwannee terrane of African origin are shown. The box delineates the area of interest shown in the larger scale map in Figure 1.2.

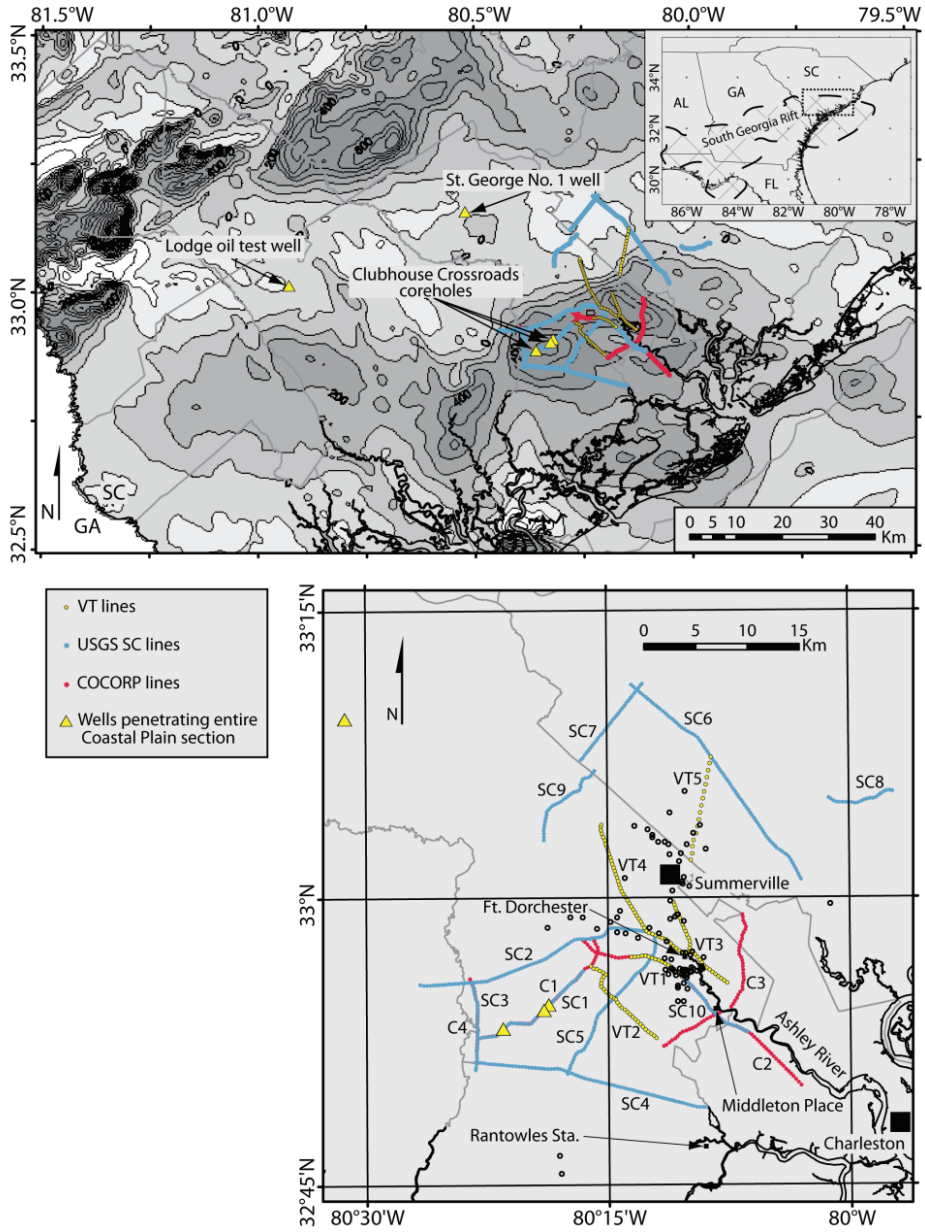

Figure 1.2: *Upper*. The contours show the total intensity magnetic anomaly (contour interval 100 nT, shading density proportional to magnetic intensity) from Daniels (2005). The inset map (upper right) shows the outline of the South Georgia Rift at regional scale as a dashed line with cross hatching and the area of the magnetic anomaly map, outlined with small circles. Yellow, blue and red filled circles show the station locations of the Virginia Tech (VT), USGS-SC (SC) and COCORP (C) reflection profiles (respectively). Yellow triangles show the locations of wells that have penetrated through the Cretaceous and younger coastal plain sediments and into rocks of early Mesozoic age. *Lower*. A more detailed map of the study area near Summerville, South Carolina. Open circles show earthquake epicenters (M > 2.0, 1977-2004) instrumentally located by the University of South Carolina seismic network. Note that profiles VT1 and SC10 overlap part of profile C2 along Ashley River road on the south side of the river. Profile C3 crosses the Ashley River near Middleton Place. Used with permission of Seismological Society of America. From Chapman and Beale, On the Geologic Structure at the Epicenter of the 1886 Charleston, South Carolina, Earthquake, Bull. Seismol. Soc Am. 100, 1010-1030, 2010, (c) Seismological Society of America.

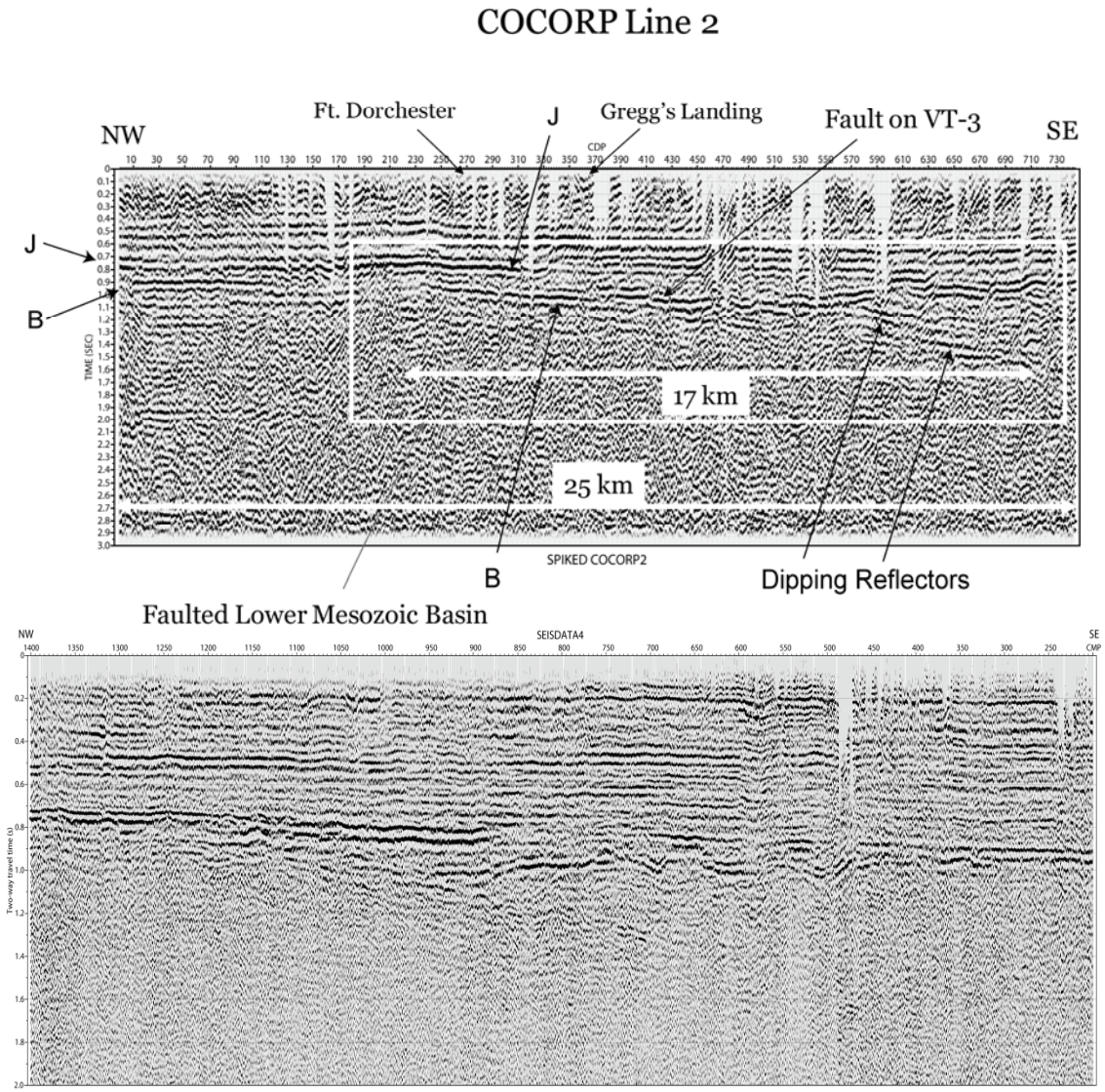

Figure 1.3: *Upper*. COCORP profile C2 collected along the southern side of the Ashley River. J and B reflections from the Lower Mesozoic section are indicated. The locations of Fort Dorchester, Gregg's Landing and the projected location of Fault C described by Chapman and Beale (2008, 2010) are indicated. Note the image of a extensive syncline-shaped structural feature involving the Lower Mesozoic section. *Lower*. CMP brute stacked section of SEISDATA4 along the part of the profile that is co-located with profile SC4 (shown in Figure 1.2). Note the similarity of the deformation involving the Lower Mesozoic section on C2 and SEISDATA4 profiles which are separated by approximately 17 km.

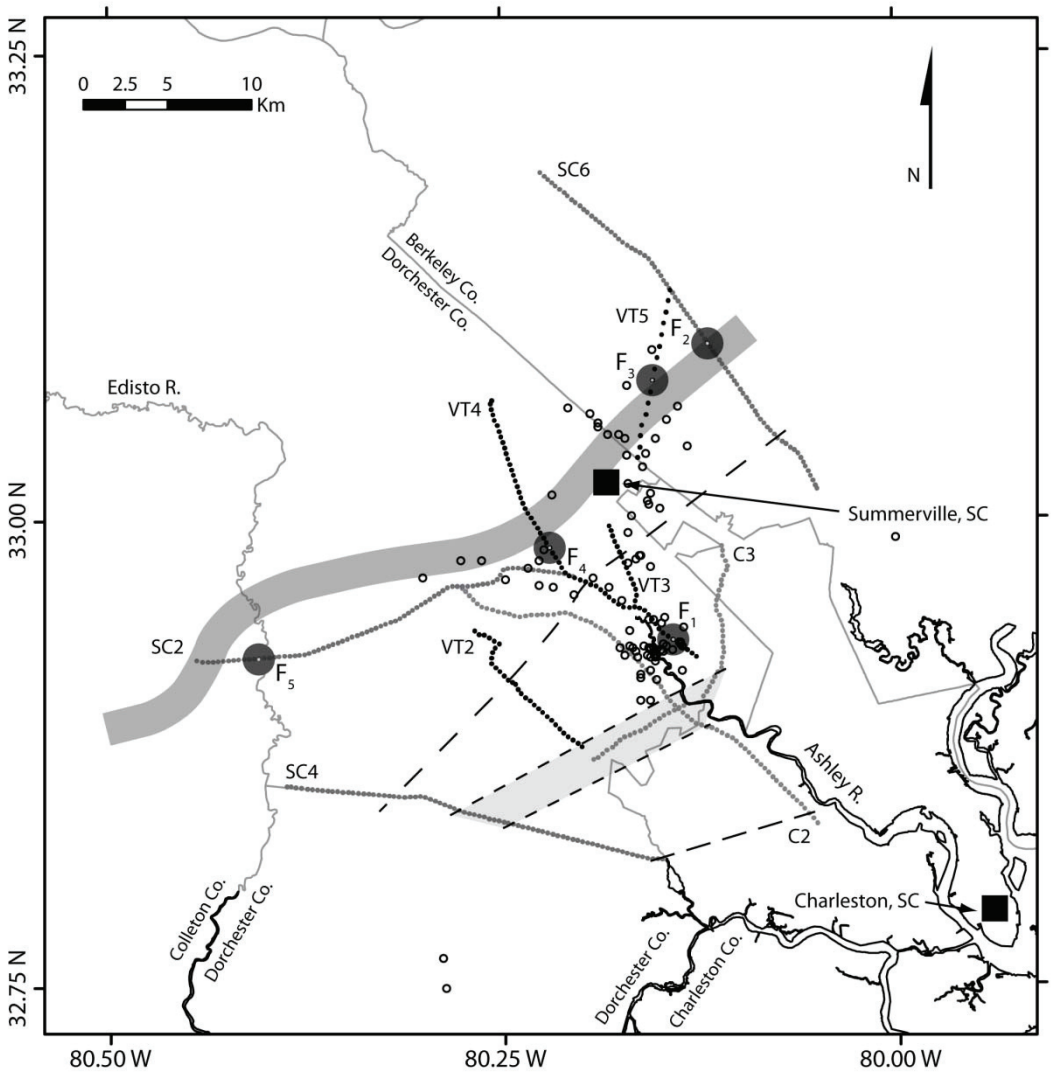

Figure 1.4: Map of the area of interest showing several geologic features. The lines composed of small dots show the locations of seismic reflection profiles (each dot is a profile station location). The location of the gradient in the magnetic field is indicated by the broad shaded line passing just northwest of Summerville, SC. The locations of Mesozoic-Cenozoic faults imaged on reflection profiles are indicated by the large filled circles, labeled F1 through F5. Small open circles show earthquake epicenters (M>2.0, occurring from 1977 through 2004) located by the University of South Carolina seismic network.The long-dashed line passing approximately 4 km southeast of Summerville marks the location where southeastward dip on the bright B reflection becomes pronounced. The long-dashed line near the end of profiles C2 and SC4 marks the location where the bright B reflection shallows to the level of the J reflection, dipping to the northwest. The trough of the intervening structural basin, defined by two-way time greater than 1.1 second for the bright B reflection, is indicated by the shaded area outlined by short-dashed lines containing the southern part of reflection profile C3. Used with permission of Seismological Society of America. From Chapman and Beale, On the Geologic Structure at the Epicenter of the 1886 Charleston, South Carolina, Earthquake, *Bull. Seismol. Soc Am.* **100**, 1010-1030, 2010, (c) Seismological Society of America.

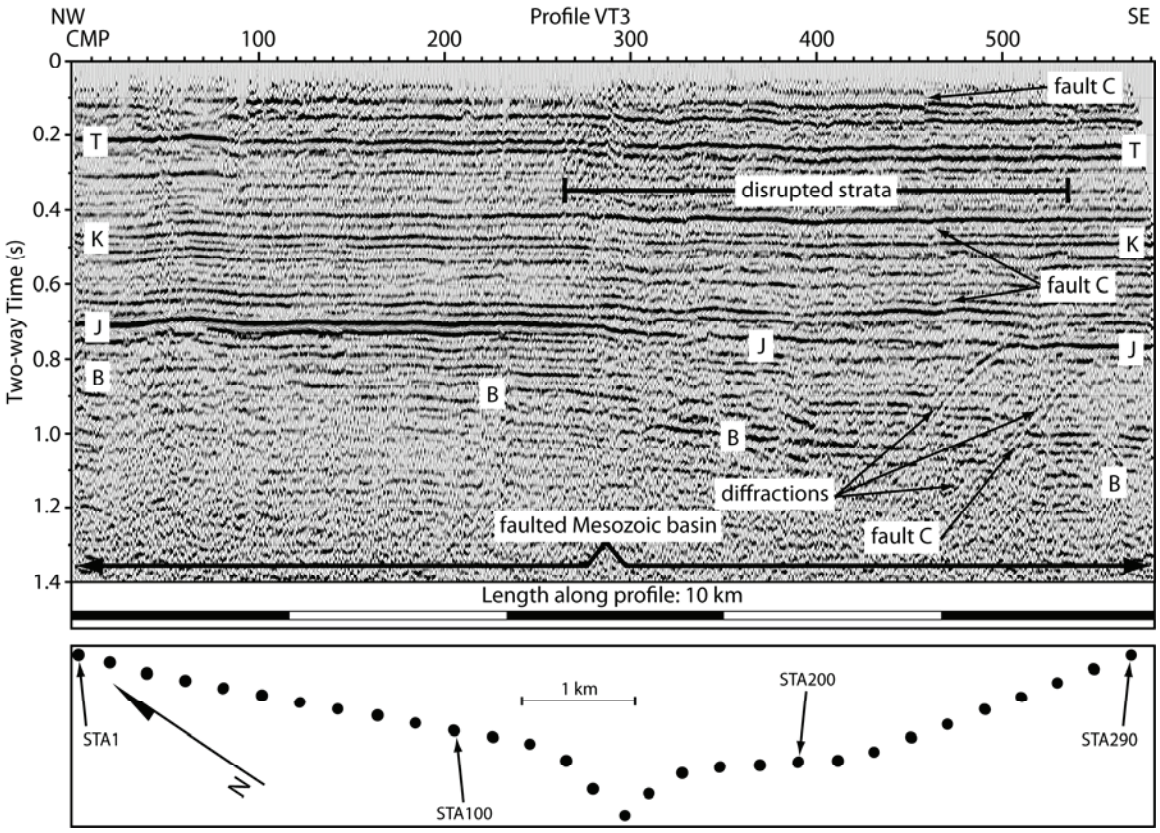

Figure 1.5: *Upper*. Reprocessed CMP stacked section of seismic profile VT3. Conspicuous reflections J and B are indicated, and are described in the text. A prominent reflection from a Tertiary unit is labeled T. A prominent reflection from a Cretaceous unit is labeled K. The arrows indicating fault C point to the best-imaged Mesozoic-Cenozoic fault in the study area. Other arrows point to the strongest examples of diffractions from the faulted edges of units. The scale bar indicates length along the actual (crooked) profile. *Lower*. Map view showing profile station locations. Used with permission of Seismological Society of America. From Chapman and Beale, On the Geologic Structure at the Epicenter of the 1886 Charleston, South Carolina, Earthquake, *Bull. Seismol. Soc Am.* **100**, 1010-1030, 2010, (c) Seismological Society of America.

Chapter 2: Data and Processing Method

Several long seismic-reflection profiles were collected in South Carolina and Georgia in 1981. These profiles, termed SEISDATA4, 6, and 8, are the result of a collaboration of the U.S. Geological Survey with other participants (Behrendt, 1986). These proprietary data are currently owned by Geophysical Pursuit, Inc. Prior to this research, these data were only available as "brute stacked" sections, published as either line drawings or low resolution images of small sections of the profiles (Behrendt, 1986). The profile studied here is a portion of SEISDATA4, which is 350 km long, extending from Charleston, SC, inland to Greenville, SC. This research focuses on the 70 km long southeastern section, which includes the epicentral area of the 1886 Charleston earthquake (Figure 2.1).

The southeast section of the profile consists of 500 VIBROSEIS sources recorded on 96 channels per source with 24 geophones per channel. Source arrays were nominally spaced at 134.2 m and receiver arrays were nominally spaced 67.1 m apart, with samples recorded at a time interval of 4 milliseconds. The spread length for individual sources was nominally 6.7 km. Maximum receiver offset was nominally 3.4 km, but varied from roughly 3 km to 4 km because of unusual source-receiver geometry. The source sweeps were 24 second, 48-12 Hz down-sweeps generated by an array of (normally) 4 truck-mounted vibrators and were repeated (normally) for a total of 16 sweeps per source. The spectrum of the source sweep is shown in Figure 2.2 and the Klauder wavelet resulting from the autocorrelation of the sweep is shown in Figure 2.3. The total record length was 32 seconds, generating an 8 second trace after standard correlation with the sweep. The recording geometry was split-spread, with a 5 station gap around the source array; however, several errors were made in the field, primarily, in positioning the source array, and documenting the actual location of the source array with respect to the

receivers. Undocumented source gaps and uneven source spacings also occurred along the profile due to obstructions such as bridges and houses. Although the source for this survey was exclusively VIBROSEIS, the term "shot" will henceforth be used to refer to sources.

2.1 Methodology

The VIBROSEIS field records (seismograms) must be correlated with a time series of the input source-energy function (source sweep) or an accurate approximation of that function, to produce time series (traces) on which distinct arrivals of seismic waves (direct wave, reflections, refractions, surface waves, etc.) can be visualized. The designed source sweep was recorded in the first channel of each shot gather and was used in the conventional manner to correlate with the field traces. This sweep trace does not precisely represent the source time-series, due to near-source effects and frequency-dependent attenuation, but it is a close approximation and generally produced good quality correlograms (traces). These traces are identical in most respects to explosion-generated traces, with one notable distinction being that the arrival times are considered to be at the maximum peak (center) of the (zero-phase) wavelet, rather than at its onset. Figure 2.4 shows representative shot gathers from SEISDATA4.

2.1.1 Geometry Assignment

The shot-receiver geometry for the profile was obtained by a careful digitization of topographic maps showing the position of every fifth station, followed by a close examination of observer's notes and shot gathers. The station locations were first digitized using the program ARCMap (available from ESRI, Inc.), followed by corrections to ensure that stations were placed along roadways and were appropriately spaced. Station locations between every fifth station were linearly interpolated, with the exception that stations around curves and sharp bends were individually digitized at the appropriate increment using measurement tools within

ARCMap. Station elevations were assigned from surveyor's notes and were confirmed by checking the elevation at various stations plotted on the topographic maps. Shot and receiver locations for each shot gather were assigned by using the correlated shot records together with the listed locations of shot and receiver positions from the observer's notes. Errors in the observer's notes created difficulty in assigning shot and receiver positions, particularly along the southeastern section of the profile. However, these issues were corrected using movement of dead or noisy stations from shot to shot, as well as gaps due to obstructions observable on topographic maps (bridges, houses, etc.). After successful geometry assignment, it became clear that errors in receiver spread placement, relative to shot location, were made during data collection. For early shots, the five-station gap around the source array was mislocated and the shot moved in an inconsistent manner relative to the receiver spread. This caused significant variation from the designed geometry for the shot gathers in this area, including varying the maximum offset from shot to shot. Shot-receiver geometry stabilizes to the normal spread geometry for later shots.

Common midpoint (CMP) numbers for crooked line geometry are assigned based on bins drawn around clusters of midpoints. All traces with midpoints within a particular bin are assigned the same CMP number. Straight-line profiles create clusters in which all midpoints are identical, whereas deviations from this, combined with the inclusion of large offsets, create clusters with points spread out over an area. Sharp bends and large offsets result in midpoints well away from the profile track, requiring larger bins to collect traces logically belonging in the same CMP bin and reducing the lateral resolution of the final image. Reducing the maximum offset mitigates this effect by tightening the clusters and reducing the area of the individual bins.

However, this reduces fold (number of traces per gather) and reduces the resolution of stacking velocities.

CMP number was assigned to each of the traces based on the location of the midpoint between source and receiver. This process is conducted in order to properly group traces with shared CMP for stacking, which produces the familiar CMP stacked-section commonly used for geologic interpretation. Two versions of this assignment were conducted producing two distinct stacked-sections: one for the shallow geologic section (two-way time less than 1 second) processed using only near offsets (Figure A.1), and another for a deeper section (two-way time les than 2 seconds) processed using all offsets (Figure A.2). Crooked-line geometry was utilized, creating CMP tracks which diverged, sometimes significantly, from the station track and from each other. This resulted in two sets of CMP numbers which do not perfectly correlate geographically (See Figure 2.1).

2.1.2 CMP Binning

Each CMP binning was created to address a certain target. Focusing on the shallow section of the Atlantic Coastal Plain (ACP) sediments, only near offsets (less than about 1 km) were included. This allowed for a CMP track that more closely followed the shot track and produced evenly populated CMP bins, but did not reduce the fold as far offsets did not include any usable reflection energy from the shallow section. Bin size was also smaller, preventing degradation of lateral resolution. For processing the deeper section, another CMP binning was created, which included the full offset range. This CMP track was significantly smoother than either the shallow CMP track or the shot track, and the bins were significantly larger. This reduces the effect of sharp bends on the final stacked section at the cost of some lateral

resolution. This is deemed an acceptable sacrifice as lateral resolution is already lower in the deeper section.

2.1.3 Trace Editing

Procedures to ensure optimum data quality were applied. Visual inspection of shot gathers revealed that offsets of more than about 1 km contained no reflection energy from the shallow sedimentary units; therefore, data beyond that offset were excluded for the shallow processing. For the deep processing, all offsets were included. Two iterations of trace kills were applied to the shallow processing; the first focused on traces that were obviously bad (i.e. extremely noisy and dead traces), allowing the second to focus on eliminating traces with subtle noise that would degrade the shallow reflections in the final stack. Only the first iteration of kills was applied to the deeper processing in order to prevent elimination of weak reflection energy that might not be easily visible on the shot gathers. A top mute (muting lateral velocities of ~1600 m/s and faster) was applied to eliminate direct and guided wave energy, as well as head waves. All mutes were tapered to prevent edge effects during later processing steps (such as wavelet shaping and frequency filtering). A bottom "cone" mute (muting lateral velocities of 200 m/s and slower) was also applied in order to eliminate surface wave energy.

2.1.4 Attenuation Correction

Geometric spreading reduces the amplitude of the expanding seismic wavefront as the wave propagates from its source. Assuming a point source, the shape of the wavefront is determined by the velocity structure of the materials in which the wave is propagating. This causes the seismic trace to be drastically reduced in amplitude with increasing time, and must be corrected during processing. There are several ways of performing an amplitude correction, producing the desired effect of boosting amplitudes at later times. Here geometric spreading

correction based on the shape of the waveform due to velocity structure was used to produce the final CMP stacked sections. This is an iterative process, as before processing is complete (i.e. – before the velocity analysis is performed), the velocity structure is largely unknown, but some amplitude correction is necessary in order to perform the velocity analysis. Therefore, an arbitrary amplitude correction is applied prior to the first pass of velocity analysis, and following the velocity analysis, a correction based on velocity structure is used for future processing runs. Prior to velocity analysis, the amplitude of the sample at each time (t) was multiplied by $t^{1.5}$ for each trace. After completion of the first pass of velocity analysis, a reasonably accurate velocity model was available for use in a more physically meaningful geometric spreading correction utilizing the model to better approximate the actual wavefront geometry as a function of time and make the appropriate correction for each trace. Although the spreading correction is time and space dependent, it is trace independent. Various factors independent of subsurface geology or the normal propagation of seismic waves can influence the mean amplitude of a trace, and often these factors lead to some traces having a significantly larger or smaller mean amplitude compared to the average trace within the data. To correct for this, a trace balance was designed to normalize the amplitude of the reflections within the zone of interest. For the shallow processing, the portion of a trace including all reflections down to the strong reflector assumed to be the Cretaceous sediment - early Mesozoic rock interface at the base of the Atlantic Coastal Plain section was compared with the same section on other traces within the gather under scrutiny. For the deeper processing, the window included times starting from this strong reflector down to about 3 seconds. This correction ensured a roughly equal contribution from each trace to the final stack for the reflections within the window, and reduced the likelihood of a noisy trace dominating the resultant stacked trace. The trace balance was applied both after all

trace independent processing was complete, and just prior to stacking, as well as prior to any visualization of gathers, such as editing traces or designing mutes. A similar trace balance was applied after stacking to improve continuity of reflectors along the stack during visualization.

2.1.5 Bandpass Filtering

At low frequencies, the most significant noise source is the surface wave (primarily Rayleigh wave on vertical seismometers). Through trial-and-error, it was determined that a high-pass filter with corner frequency 16 Hz significantly reduced surface wave amplitudes and improved the overall appearance of the traces even outside of the surface wave cone. Examination of the frequency spectrum of the traces within the shallow zone of interest (two-way time less than 2 seconds) revealed that the sweep was heavily attenuated above 40 Hz (Figure 2.2B). A low-pass filter with corner frequency 40 Hz was applied and significantly improved the overall signal-to-noise ratio of the time domain data. The previous frequency-band analysis resulted in a band-pass filter of 16-40 Hz with 18 dB/Hz slopes. This is the equivalent of a 3 pole filter which is a good trade-off between strong reduction of energy outside the pass band and minimal ringing from the sharp edge of the filter in the frequency domain (Gibbs effect). The band-pass filter, in concert with the mutes described above, effectively reduced noise on the traces (Figure 2.4).

2.1.6 Minimum Phase Correction and Spiking Deconvolution

Autocorrelation of a linearly-swept, band-limited signal produces a wavelet referred to as a Klauder wavelet. This wavelet is zero-phase, which makes it symmetric, and the number and character of its non-negligible side lobes is determined by the frequency content of the auto-correlated signal. The (truncated) Klauder wavelet due to the autocorrelation of the SEISDATA4 sweep is shown in Figure 2.3. Every reflection recorded on the traces is a

reflection of the entire sweep (or at least an attenuated version of the sweep), and cross correlation of the traces with the sweep produces a (distorted) Klauder wavelet at the arrival time of each reflection. The finite width of the non-negligible portion of the wavelet makes it difficult to discern interfering reflections within this time interval. Therefore, it is desirable to filter the traces in such a way that reduces the width of the wavelet as much as possible. The process of accomplishing this purpose is termed deconvolution. Deconvolution attempts to compress the wavelet into an idealized zero-lag spike.

A discussion of deconvolution as applied to Vibroseis data is given by Yilmaz (1987): the main points are summarized here. The process of deconvolution is derived from the idea that the recorded seismic trace $x(t)$ is comprised of three basic independent components:

$$x(t) = w(t) * e(t) + n(t), \qquad (2.1)$$

where $w(t)$ is the wavelet including the effects of source, travel path, and recording system, $e(t)$ is the subsurface reflectivity series (earth's impulse response), $n(t)$ is noise. Note that the "wavelet" is not strictly a function of the source, and is not equivalent to the Vibroseis source sweep. In Equation 2.1, * denotes convolution (Yilmaz, 1987). The goal is to determine the unknown $e(t)$ from the known $x(t)$, but obviously unknowns $w(t)$ and $n(t)$ must be treated first. The deconvolution process as usually implemented involves the following set of assumptions (Yilmaz, 1987): 1) Normal incidence, compressional plane waves from the source (no shear waves) that reflect from horizontal, constant velocity layers in the subsurface (zero-offset recording); 2) The source does not change its character with time (stationarity); 3) The noise component, $n(t)$, is zero; 4) The source component, $w(t)$, is known or can be approximated; 5) The reflectivity series, $e(t)$, is random; 6) The wavelet $w(t)$ has a stable inverse. These assumptions have the following implications (Yilmaz, 1987): 1) Non-zero offsets must have ray

paths steep enough to be approximated as zero offset (farther offsets can be included for deeper reflections); 2) Since the source does change its character significantly with time, some correction must be applied, or the trace must be effectively divided into shorter time segments which each contain a roughly stationary wavelet, as described below in the procedure for spiking deconvolution used here; 3) Noise must be reduced using frequency filtering as detailed above, and noise remaining after filtering must be neglected; 4) *w(t)* must be estimated from the seismic trace as described below; 5) The Fourier amplitude spectrum of the seismogram *x(t)* and *w(t)* are similar (i.e., bandwidth and general functional shape), allowing the autocorrelation of the seismogram *x(t)* to be substituted for *w(t)*, in the predictive deconvolution procedure; 6) The inverse of *w(t)* is minimum phase, making it stable as (as opposed to the inverse of both mixed-phase and maximum-phase wavelets, which are not stable). The Vibroseis source is not minimum phase; consequently *w(t)* is not minimum phase.

It is possible to develop an inverse of the wavelet, *w'(t)*, using a process such as the least-squares method, which when applied to the noise-free seismogram, *x(t)*, produces the subsurface reflectivity series, *e(t)* (Yilmaz, 1987):

$$e(t) = w(t) * w'(t) * x(t), \qquad (2.2)$$

where *w'(t)* is the inverse of *w(t)* and their convolution produces the Dirac function, $\delta(t)$ (a zero-lag impulse), and the remaining terms are as defined above in Equation 2.1.

Equation 2.1 can be re-written to explicitly incorporate the Vibroseis source sweep.

$$x(t) = s(t) * v(t) * e(t) + n(t), \qquad (2.3)$$

where *s(t)* is the (assumed) known source wavelet (sweep), *v(t)* is attenuation path and receiver effects, and the remaining terms are as defined above in Equation 2.1. Assuming that $n(t) = 0$

cross-correlation of the seismogram, *x(t)*, with the sweep, *s(t)*, produces the Vibroseis correlogram, or trace *x'(t)* (Yilmaz, 1987):

$$x'(t) = k(t) * v(t) * e(t) \qquad (2.4)$$

where *k(t)* is the Klauder wavelet, as described above, and the remaining terms are as defined above in Equations 2.1 and 2.3. As noted above, the Klauder wavelet is zero phase, and it can be shown that the Earth's impulse response is minimum phase (Telford, Geldart, Sheriff, Applied Geophysics p 227). The convolution of a zero-phase series and the assumed minimum-phase series produces a mixed-phase series, which as previously noted, has an unstable inverse and is unacceptable with regard to the spiking deconvolution process. Minimum phase conversion is accomplished with the use of the Hilbert transform. The minimum-phase-conversion operator was designed using the truncated, tapered Klauder wavelet of Figure 2.3 as input. Filter parameters were designed based upon the effective conversion of this wavelet into a minimum-phase counterpart. The same minimum-phase filter was then applied to the traces prior to deconvolution.

Two procedures were used before deconvolution to help alleviate the violation of assumption 2 above due to anelastic absorption as the wave travels through the sediments of the Atlantic Coastal Plain. A limited Q-correction, using a Q value of 80 based on previous estimation of Q for P-waves in the Atlantic Coastal Plain in Virginia (Chapman et al., 2008), was applied prior to deconvolution. Absorption significantly attenuates the higher frequencies of the sweep causing the wavelet to be distorted at late times compared to early times. The correction was limited in order to reduce the inevitable amplification of noise present at the higher frequencies of the sweep. Wavelet non-stationarity was further reduced by designing more than

one deconvolution operator over shorter time intervals, as mentioned above and described more completely below.

Spiking deconvolution was determined to be most useful for the shallow processing, and therefore, spiking-deconvolution filters were designed based on characteristics of the early times of the seismic traces. Visual examination of the time-varying wavelet led to the division of the traces into two shorter sections for the purpose of designing the filter operators. The first included all reflectors judged to be within the ACP and the second included the strong reflector judged to be the base of the ACP and overlapped the first window by 50 milliseconds. The operator length of 72 ms for both filters was based on the examination of the autocorrelations of the seismic traces, according to the method described by Yilmaz (1987). A small amount of "white" noise was added to the amplitude spectra prior to the inversion in order to stabilize the computations. The result was sensitive to adjustments in these parameters, but appeared to be somewhat sensitive to adjustments in the operator length. Significantly shorter operator lengths did not sufficiently compress the wavelet, leaving the traces looking "ringy". Significantly longer operator lengths tended to introduce spurious noise into the resultant trace while not improving the wavelet compression, as described by Yilmaz (1987). While the spiking deconvolution was successful in significantly compressing the wavelet, the idealized spike was not obtained due primarily to the limited bandwidth of the source, as well as to the existence of significant levels of noise. The result of the spiking deconvolution on two representative shot gathers can be seen in Figure 2.4.

2.1.7 Velocity Analysis

A Root-Mean-Square (RMS) (stacking) velocity model was created using a combination of semblance analysis and hyperbola fitting of CMP gathers (Figure 2.5). Prior to their use in the

velocity analysis, CMP gathers were partially processed including muting, trace killing, frequency filtering, but not deconvolution. Deconvolution has the effect of decreasing reflection strength while improving temporal resolution, so it was not applied for the velocity analysis where temporal resolution is not as important. An AGC amplitude adjustment was applied in order to equalize the amplitudes of different reflections and offsets. An increase in fold was accomplished by combining three CMP gathers into a new "supergather", with supergathers spaced at a ten CMP increment. The increase in fold was gained at the expense of both spatial and temporal resolution. This is deemed an acceptable trade-off, because the resolution is not needed for the purpose of velocity analysis. The nominal CMP fold is 24 traces, but due to the abnormal geometry of some shots, as well as the crooked-line CMP track discussed above, the fold varied greatly and the maximum fold for any CMP gather is 47 traces for the shallow processing. The fold was reduced for the shallow processing by excluding all offsets greater than 1 km. This was done because no reflection energy from the sedimentary section is present at these farther offsets. Semblance is generally calculated at each velocity step by normal-moveout correcting the gather using the given velocity and then measuring the power of the amplitudes at each given time step. The process is repeated for each velocity and the results are plotted together on a single panel (Figure 2.5B). Velocity-time coordinates that have good coherence of amplitudes plot as large values and these are desired to be distinct peaks representing the correct velocity for that time at that CMP. This approach is coupled with the hyperbola fitting approach, in which the hyperbola corresponding to a given velocity is plotted over the CMP gather (or supergather), and when a match between the picking and reflection hyperbolas is seen, the correct velocity is picked. This can be done dynamically with the ProMax software on the computer screen showing both the gather and the corresponding

semblance panel. The cursor is moved over the semblance panel (representing a map of time-velocity) and the appropriate hyperbola for the cursor's present time-velocity is plotted on the gather. This is the approach that was used here, which allowed both techniques to be used in tandem. The semblance values for the shallow processing were calculated at a velocity interval of 100 m/s from 1000 m/s to 3000 m/s, and a time interval of 20 ms from 0 s to 2 s, using a 120 ms moving time window. This window length was large enough to include the entire wavelet, but small enough to generally prevent the inclusion of more than one reflection. Similar parameters were used for the deeper processing, except that all offsets were included and velocities up to 3,500 m/s were scanned. Reflectors were picked down to the strongest reflection on the records (1000 ms at CMP1, 700 ms at CMP 2000), which is interpreted to be the reflection from the base of the ACP. CMP gathers with low velocity resolution were ignored to prevent deterioration of the quality of the analysis. During analysis NMO correction was also applied to help determine best fitting for hyperbolic move-out and semblance. After the velocities were picked using the technique described above, the resulting model was lightly smoothed in CMP-time space to reduce artifacts from sharp changes in velocity. This smoothed model is used to produce the final CMP stack as described below.

2.1.8 CMP Stacking

The final CMP stack is produced by horizontally stacking the NMO-corrected, fully pre-stack-processed CMP gathers. The gathers were NMO corrected and stacked according to the normal convention. For the shallow processing, only the first second of the data were included in the final stack.

2.1.9 Refraction Analysis of the Lower Mesozoic Section

Refraction velocities were calculated from as many shots as possible along the line. Travel time picks were measured from arrivals determined to be the refraction from the top of the lower Mesozoic rock at the PRU, at offsets ranging from 2100 m to 3050 m. It is important to note that the picks were often not the first strong arrival. This proved to be a difficulty in some areas because of the low data quality, crooked profile, and complex geologic structure of the early Mesozoic units beneath the PRU. Several examinations of the picks were needed to insure their accuracy. Refracted arrivals from layered structure theoretically have linear move-out; therefore, the picks were all selected to be the linear fit that best represented the refraction velocity of the chosen arrival. However, in many cases, the arrivals exhibited small offsets in the arrival times of the refraction, shown by an example in Figure 2.6. Dealing with this effect proved difficult or impossible in the most tectonically disturbed section of the profile near Rantowles (Figure 3.1).

The reflection inferred to mark the PRU has a regional SE dip on the common midpoint (CMP) stacked section of SEISDATA4 (Figure A.2). Detailed examination revealed that variable local dips can be observed over small offset range: this affects the apparent velocities of picked arrivals along the profile. A dipping interface causes an increase in the velocity measured in the up-dip direction, and a decrease in the down-dip velocity; therefore, both “forward” and “reverse” directions were measured. The forward and reverse measurements were reconciled based on a close match between the center CMP of the offset ranges for each direction. The corrected velocity obtained from a single match of forward and reverse measurements was positioned at that central CMP. These corrected velocities were obtained using the classic dipping layer model where the refraction velocity of the dipping layer is:

$$V_2 \cong 2\left(\frac{V_d V_u}{V_d + V_u}\right)$$

Where V_2 is the corrected refraction velocity and V_d is the velocity in the down-dip direction and V_u is the velocity in the up-dip direction. Note that this approximation works only for instances where the dip on the layer is "small" (i.e. less than 10 degrees) which holds in this case.

Interval velocities derived from the reflection hyperbola of the reflection from the PRU and the next deeper reflection hyperbola served as a check on the refraction velocities. This interval velocity analysis was done using a few shots along the line, to check for consistency with the refraction velocity estimates.

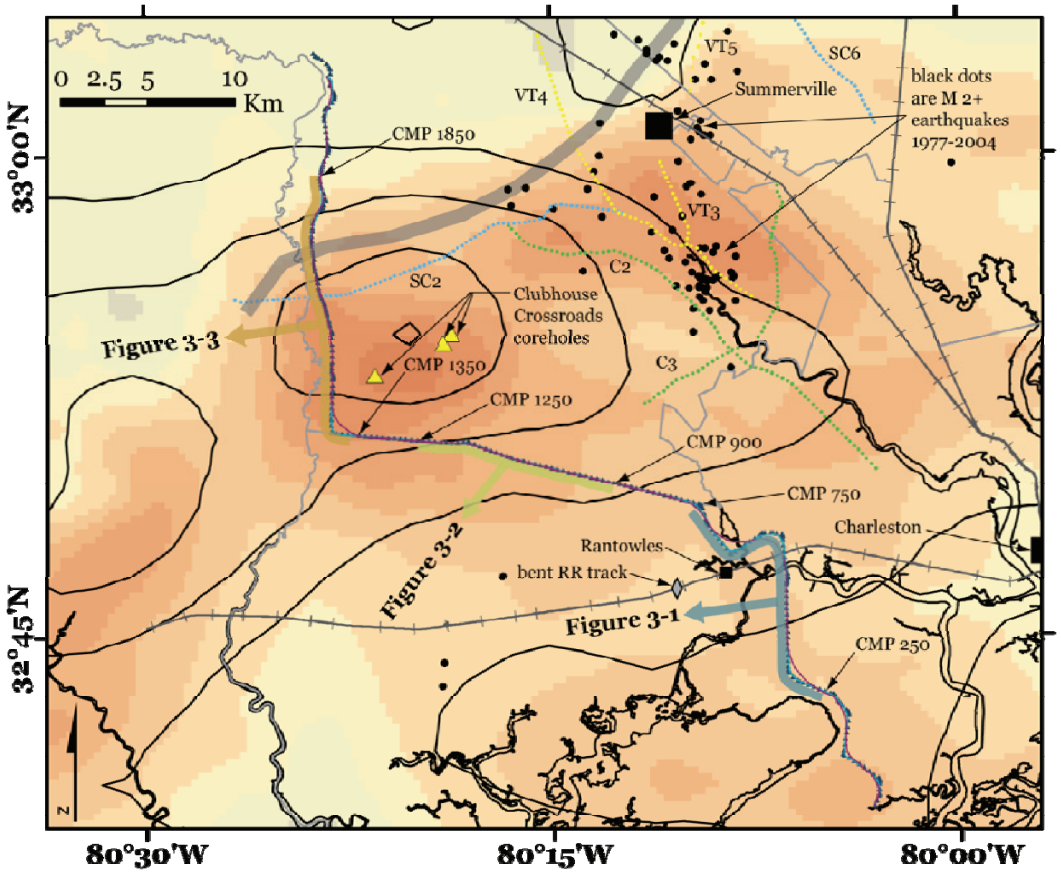

Figure 2.1: Map of study area. Colored contours show total intensity magnetic anomaly (dark- large values: light - small values). Solid line contours show Bouguer gravity anomaly, with largest values spatially associated with large magnetic anomaly values. The thick grey line shows the location of the magnetic gradient separating a zone of low intensity to the northwest from the magnetic high to the southeast. Small filled circles show epicenters of earthquakes with magnitudes greater than 2.0 in the 1977-2004 time period. Colored dots show the station locations for several seismic reflection profiles re-processed and described by Chapman and Beale (2008, 2010). Sections of profile SEISDATA4 described in detail in the text are indicated by the thick colored lines, with arrows referring to Figure numbers showing the stacked record sections.

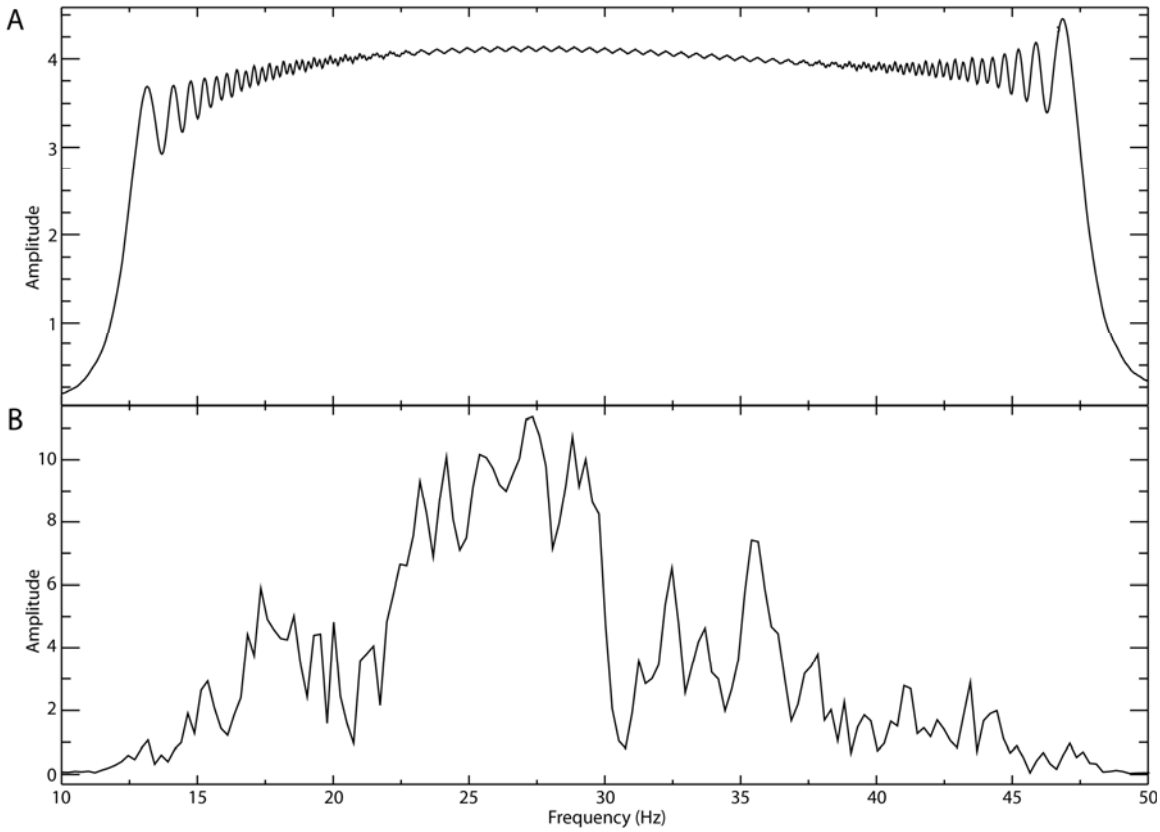

Figure 2.2: (A) Fourier amplitude spectrum of the 48-12 Hz Vibroseis source sweep. (B) Fourier amplitude spectrum of the first 2 seconds of an arbitrary correlated seismic trace from profile SEISDATA4.

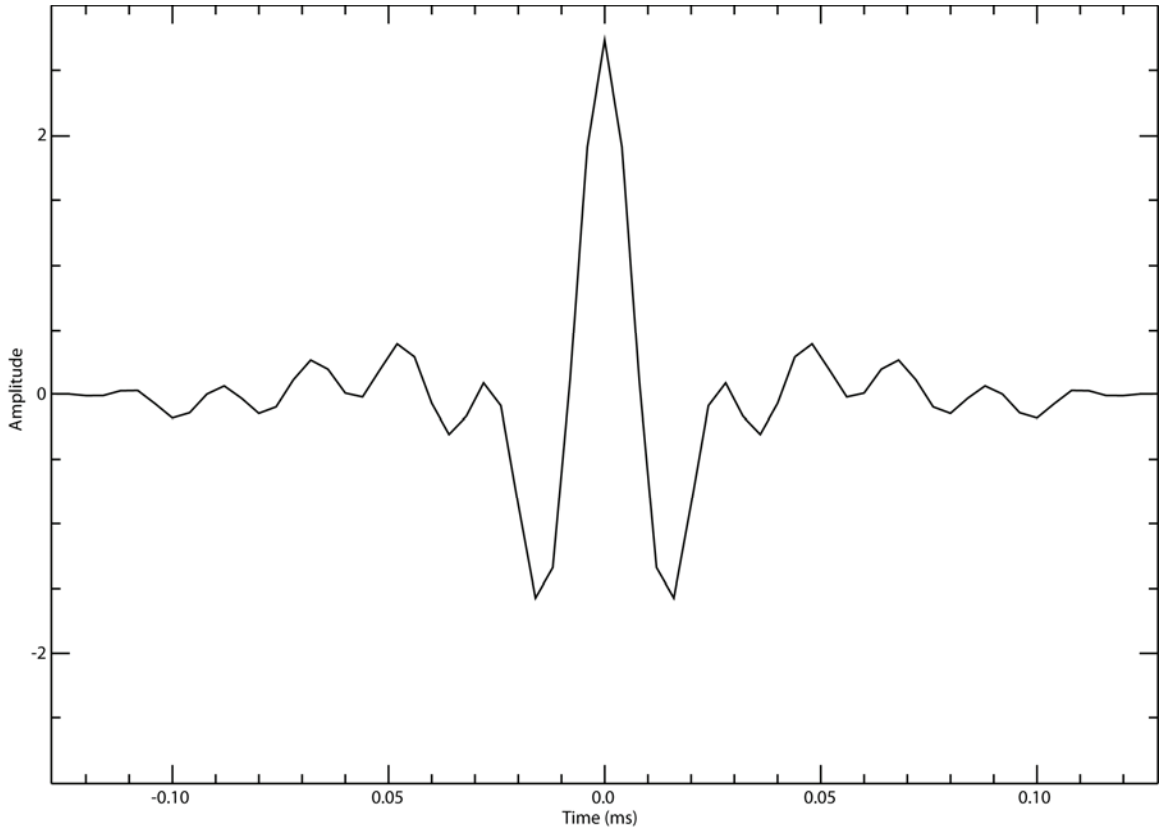

Figure 2.3: The two-sided Klauder wavelet resulting from the autocorrelation of the source sweep, truncated at 256 ms with a 32 ms taper applied to each end.

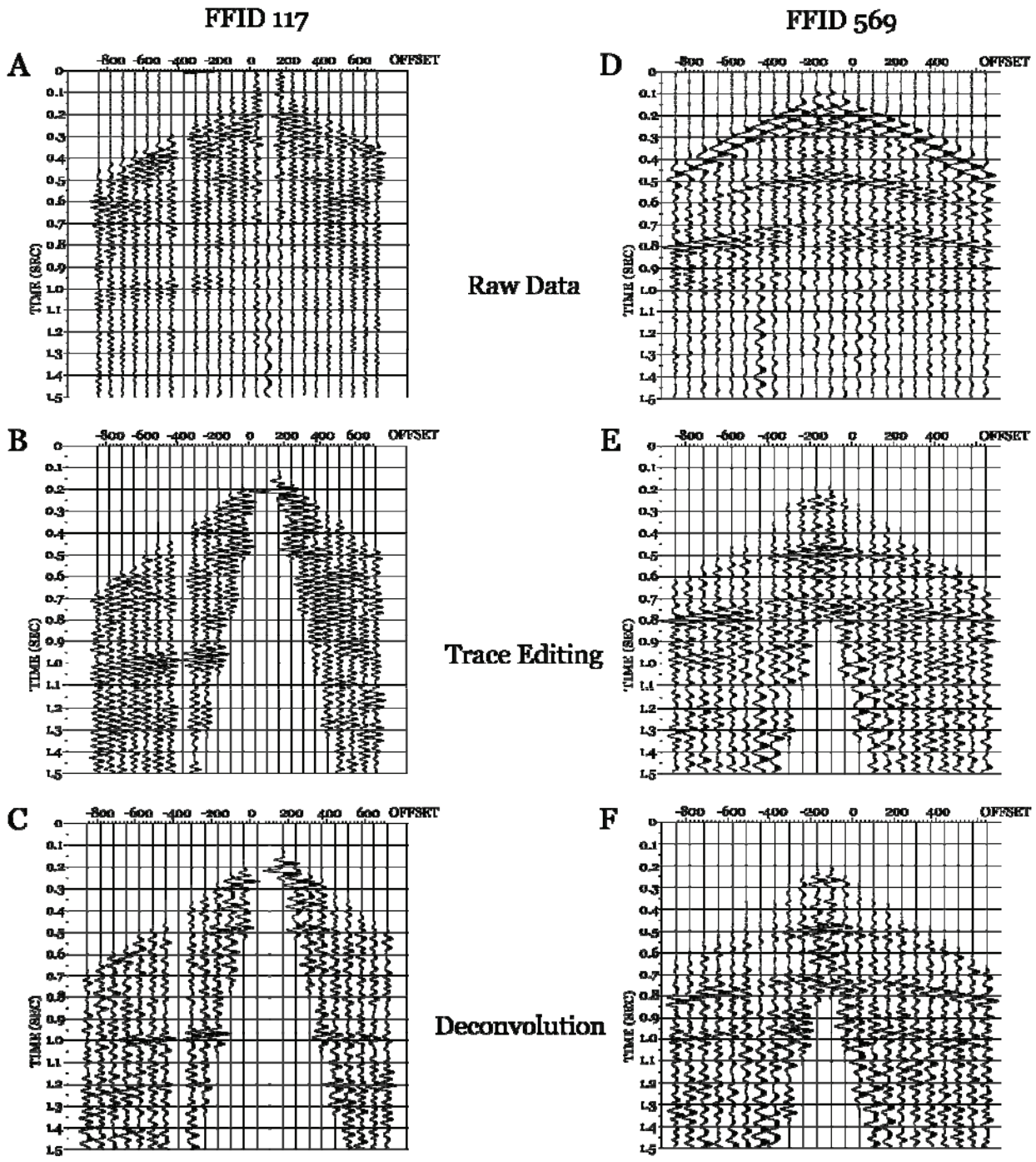

Figure 2.4: Three stages of processing. Left column (plots A, B and C) are shot-gathers from the southeastern end of SEISDATA4. The right column of plots (D,E and F) are shot-gathers from the northwestern end of the profile. Plots in the left column show the results of raw sweep correlation (A), the results of applying trace kills, top and bottom mutes and bandpass filter (B), and both previous stages plus minimum phase conversion and spiking deconvolution (C). The same processing stages are show in the right column, respectively, in plots D, E, and F for the northwestern profile shot-gather. Note that the data quality in the right column (northwestern part of profile) is much better than for the left column (southeastern part of profile). This is generally the case with other shot gathers, and hence, geologic structure along the northwestern half of SEISDATA4 is better resolved.

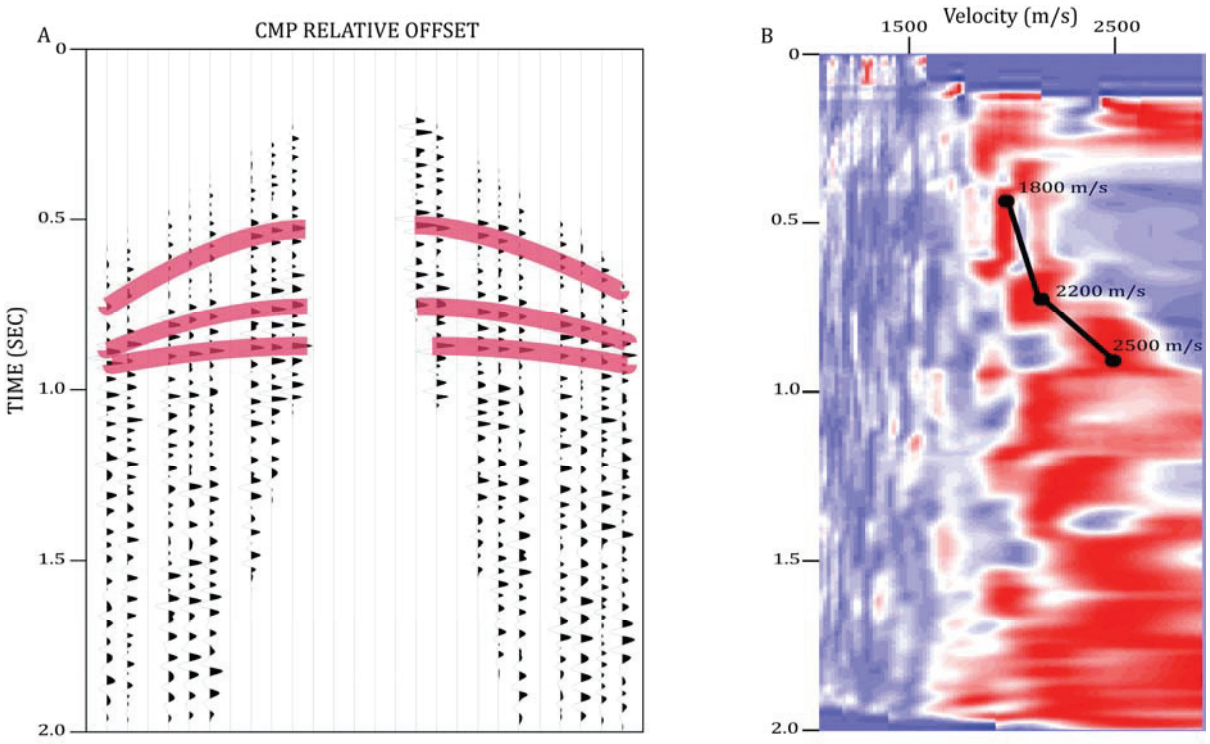

Figure 2.5: (A) CMP supergather. (B) Corresponding semblance plot. The CMP supergather is the combination of 3 consecutive CMP gathers with limited processing applied. The semblance plot shows a measure of coherency of reflection energy along hyperbolic paths calculated at a 50 m/s increment in velocity and 20 ms increment in time using a 120 ms time window. The circles on the semblance plot and the hyperbolae of the supergather plot indicate velocities picked from the analysis.

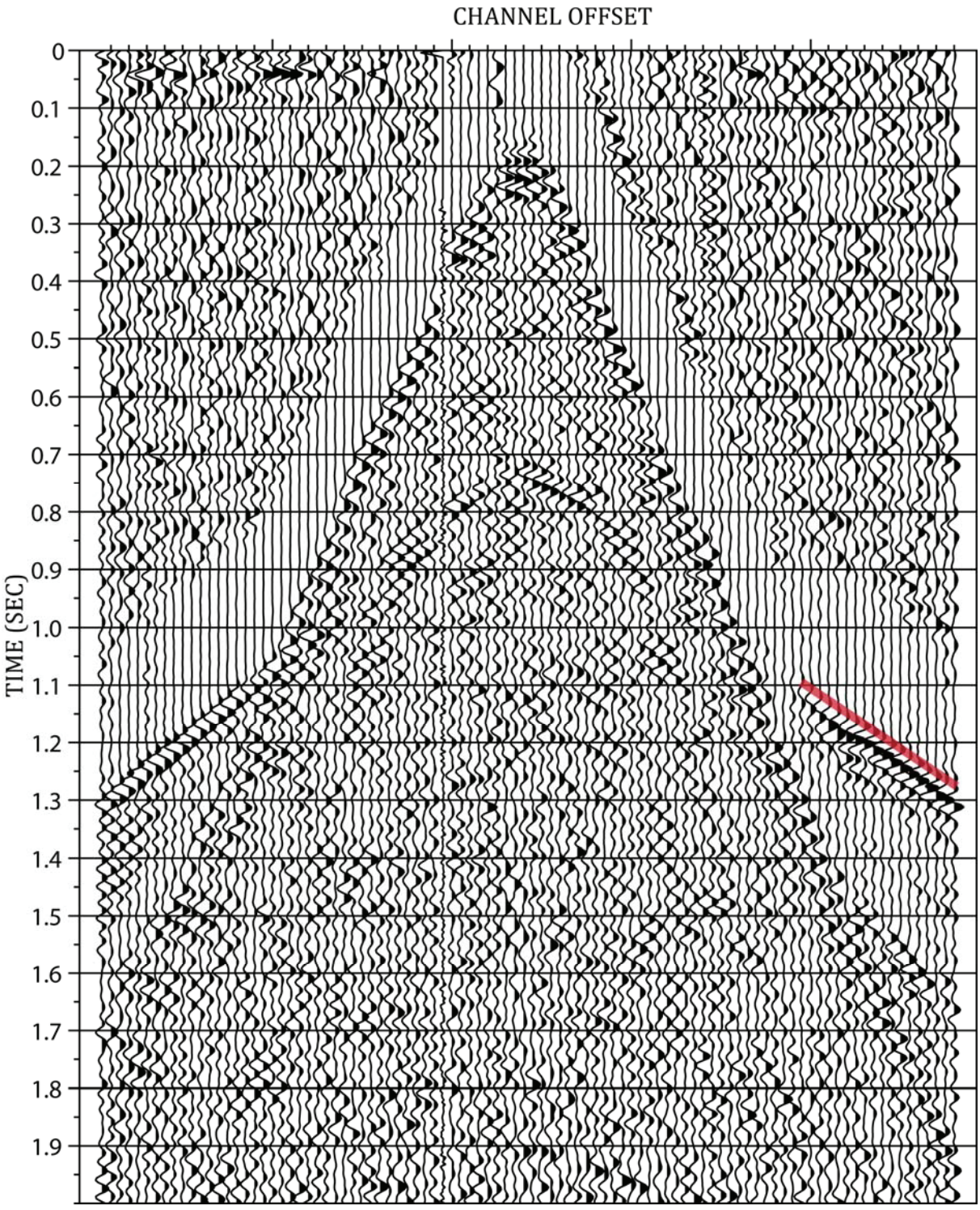

Figure 2.6: Representative shot gather showing arrivals interpreted to be refractions from the sediment-rock interface at the base of the Atlantic coastal plain section. Note an abrupt offset of refracted arrivals (shifted earlier in time with increasing offset), a phenomenon often observed in association with faults. Red line represents refraction analysis picks. Bandpass filter and AGC have been applied.

Chapter 3: Results and Discussion

3.1 SEISDATA4 Re-processing

The re-processing of seismic reflection profile SEISDATA4 produced a successful stack of the southeastern most section of the line. Detailed descriptions of important features imaged on SEISDATA4 will be described in later sections. Figures A.1 and A.2 show the full CMP stacks of from 0 to 1 seconds, and from 0 to 2 seconds. The data quality varied greatly across the line, and some poor quality areas suffered much loss of fold. This variation in quality was mostly due to high cultural noise, odd line geometry, human error (incorrect source-receiver geometry), and undocumented changes in the source sweep (such as reduction in sweep energy).

Three continuous reflectors are observable within the shallow section, represented by the first one second of data. The shallowest units visible on the stacked section at approximately 200 ms two-way travel time correspond to a depth of ~180 meters assuming a velocity of 1800 m/s . Offsets due to faults cannot easily be resolved unless the reflectors are imaged as laterally continuous features. Thus the main goal of the processing of the upper one second of data was to produce a stack that showed areas of reflector continuity in the coastal plain. While there are areas of poor data quality the continuity of reflectors is not completely lost. The profile stacks contained in the Appendix show that the range from CMP 1-500 is an area of generally good data quality with only one major data gap centered on CMP 250. Continuity of reflectors above 600 ms is lost briefly but can be traced across this zone. The largest data gap occurs between CMP 500-550. This is attributed to inconsistent shot geometry and overall poor data quality throughout this section. The gap itself is present through the entire 1 second stacked section. The overall quality of the data is greater as the line continues to the northwest. Data gaps are not present after CMP 550 and the shot geometry becomes consistent.

3.2 Deformation Imaged on SEISDATA4

There are three features of particular interest on the profile. The features will be discussed in sequence, from the southeastern end of the profile to the northwest.

Evidence for deformation of Cretaceous-Cenozoic sediments appears near CMP 600 at a time just less than 500 ms (Figure 3.1). Here a monocline fold in the reflectors is obvious, beyond which the reflectors return to a more horizontal geometry. Another fold is apparent to the east, at approximately CMP 550. The lower Mesozoic section below these folds exhibits lateral truncation of units and changes in apparent dip consistent with disruption by faulting. Two Mesozoic-Cenozoic faults are interpreted here at CMP 600 and 550, as indicated by dashed lines in Figure 3.1. However, the interpretation is complicated by the fact that the profile in this area undergoes a series of bends, and was obstructed by surface features including a bridge. As a result, some of the disruption attributed to faulting may be due to changes in apparent dip due to change in profile orientation and artifacts introduced by loss of fold in the stacked section.

Further to the northwest, beyond Rantowles, between CMP 950 and 1250, the reflections exhibit a sequence of minor folds that are interpreted here as evidence for Mesozoic-Cenozoic faults (Figure 3.2). The deformation is very subtle, and is apparent primarily as minor warping and folding of the brighter coastal plain sediment reflections at approximately 0.5 seconds two-way time. The underlying early Mesozoic section appears to be similarly affected. The fault interpreted here at CMP 1180 on SEISDATA4 corresponds with a feature previously noted by Hamilton et al. (1983) on co-located seismic profile SC4, which they named the Drayton Fault. The image obtained by reprocessing SEISDATA4 provides much better resolution of this feature than was previously available, and it shows that the Cenozoic faulting is not confined to a single fault, but to a series of faults with minor deformation along this section of the profile. Here, the

Cretaceous-lower Mesozoic unconformity (PRU) is marked by the strong reflection from the lower Jurassic J basalt.

A third area of Cenozoic deformation is seen in the CMP range 1500 to 1850 (Figure 3.3). This section of the profile has very high-quality data, and exhibits the best resolved evidence of Cenozoic deformation. At CMP 1780 there is a monocline down-to-the-south fold that involves the coastal plain units as well as the lower Mesozoic section. This general style of deformation, resolved here as folding, continues along this section of the profile, from CMP 1780 to 1500. The reflectors in the vicinity of 0.5 seconds two-way time are clearly involved. However, the shallowest reflection, resolvable at approximately 200 ms, shows less deformation. Overall, the disturbed section of the profile shows clear evidence of a general down-to-the-south displacement between several high angle faults, as interpreted in Figure 3.3. The deformation observed on this section of SEISDATA4 is similar to that noted on other profiles that cross the magnetic gradient in the study area, particularly, VT4 and VT5, which are shown for comparison in Figures 3.4 and 3.5, respectively. This section of SEISDATA4 crosses the magnetic gradient, which is coincident with the location of the observed deformation.

3.3 Refraction Analysis

The main purpose of the refraction analysis was to gain an understanding of the lithologies present at the base of the coastal plain section along the SEISDATA4 profile. These lithologies can be interpreted from velocities. This is the only method available for an appraisal of local lithology, because well control directly along the profile is absent.

The methods applied for the refraction analysis are described in Section 2.1.9. The results are shown in Figure 3.6 including both measured velocities (forward and reverse) and corrected velocities where CMP matching was possible. There is a gap in the central portion of the profile

(CMP 200-1000) where refractions from the PRU could not be clearly identified on the shot gathers due to intervals of poor data quality and the existence of a zone of strong tectonic disturbance of the lower Mesozoic units. It is clear that the sub-PRU velocity on the two sides of this zone of tectonic disturbance is significantly different. Velocities on the southeastern portion of the line (CMP 1-200) are in the range 4200 +/- 500 m/s. The sub-PRU velocity on the northwestern portion of the line (CMP 1000-1900) is significantly greater: 5500 +/- 500 m/s. This represents a difference of about 1300 m/s. Although local velocity variations appear along the profile, they are small compared to the 1,300 m/s/ difference between the mean velocities on either side of the zone of early Mesozoic tectonic disturbance.

Interval velocities calculated from the SE to the NW along this survey revealed results consistent with the refraction analysis. A lower interval velocity (~5000 m/s) is observed along the southeastern section (CMP 1-195), while along the northwestern section (CMP 1000-1900) the interval velocity is ~5800-6000 m/s. Calculations were also made in the area of low data quality where refraction picks were impossible. This area also revealed lower velocities (~5000 m/s) similar to the range observed along the southeastern section.

The refraction velocity analysis has led to two interpretations: (1) the evidence of significantly different refraction velocities between the NW and SE portions of the profile suggests that towards the southeastern end of SEISDATA4, the lithology of rocks underlying the coastal plain sediments is different from that to the northwest, and (2) local variations of the refraction velocity at the base of the coastal plain section to the northwest may be data artifacts or may be differential weathering and/or minor faulting of the PRU.

Regional well-control relevant to this profile consists of six wells penetrating the PRU in three general locations as seen in Figure 1.2. The most relevant wells are the three Clubhouse

Crossroads coreholes (CCC1-3) located within 5 kilometers of SEISDATA4 (Higgins et al, 1978). All three wells encountered basalt at the PRU with CCC3 continuing through 250 meters of basalt layers and thin sedimentary rock layers and bottoming out in "red bed" rift-related sedimentary rock (Gohn 1983). Another well located near the town of St. George, SC 20 kilometers to the North of CMP 1900 also bottomed in basalt at the PRU (Reid et al. 1986). A "wildcat" oil test well in Lodge, SC 30 kilometers to the NW, did not encounter basalt at the PRU, but did penetrate ~3 km of alternating "red bed" sedimentary rocks and basalt/diabase units and bottomed in basalt/diabase (See Chapman and Beale 2010 for discussion of that well).

Well control is absent along the southeastern end of SEISDATA4, therefore it is impossible to definitively identify the sub-PRU lithology along that section. However, on the basis of the well data throughout the SGR , and experience from exposed Mesozoic basins in the Appalachians, there are two main lithologies present within the SGR; mafic volcanic rocks (basalt or diabase), and clastic "red bed" rift-related sedimentary rock. These two types of rocks differ distinctly in velocity with "red beds" being typically in the 3500 - 4500 m/s range and unweathered basalt being higher than 5000 m/s (Carmichael, 1982). This lends itself to the interpretation that at the southeastern end of the profile, where velocities were consistently measured around 4200 m/s, the early Mesozoic rocks underlying the Atlantic coastal plain sediments are probably red beds.

Northwest of CMP 1000, it is clear from the shot gathers that the refraction velocity of approximately 5500 m/s is significantly higher. This velocity is representative of a weathered basalt, which as noted above was found at the PRU in several wells in the vicinity, including the three wells near Clubhouse Crossroads (CCC1, 2 and 3) located only 5 km from CMP 1350 (Figure 2.1). This part of the CMP stacked section also shows the best example of the strong

reflector, typical of the “J basalt". The velocities determined along the profile from the refraction analysis, and the changing character of the reflection from the base of the coastal plain section suggests that the “J basalt” terminates near CMP 1000 on SEISDATA4. The nature of the apparent cyclic velocity variations observed along the northwest section of the profile is not fully understood. It may be the result of a combination of sampling artifacts and local weathering and/or minor faulting of the “J basalt.” The presence of faults is corroborated by the raw shot gathers showing offset of the refraction arrivals (Figure 2.6).

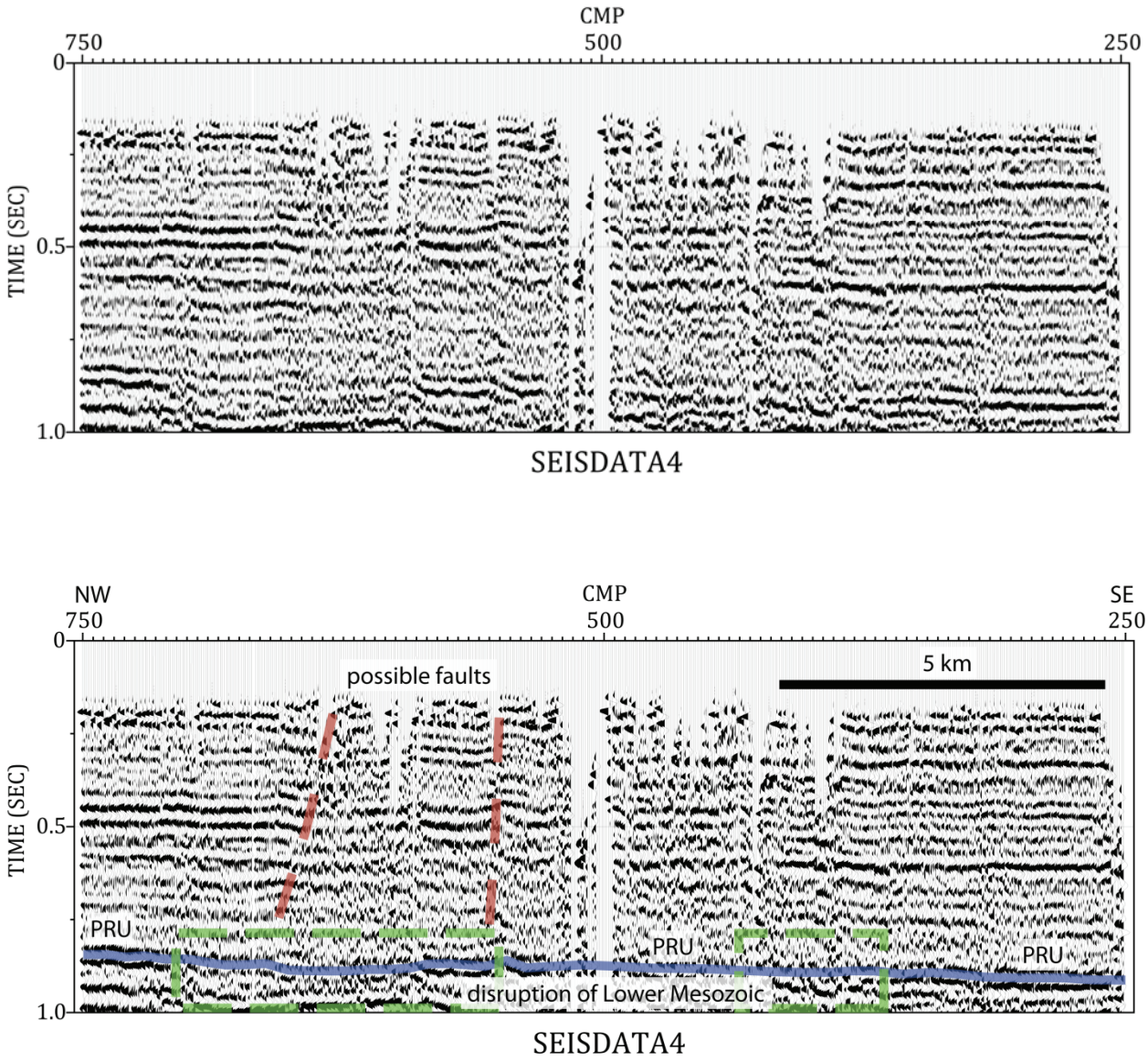

Figure 3.1: Reprocessed SEISDATA4 profile between CMP 250 and 750, near Rantowles, South Carolina. Refer to Figure 2.1 for location map. The dashed red lines indicate interpreted faults affecting the coastal plain sediments at times less than 0.75 seconds. The contact between the Cretaceous and younger coastal plain sediments and the lower Mesozoic section (post-rift unconformity: PRU) is indicated by blue line. In this section of the profile, the bright J reflection marking the PRU is missing, and the lower Mesozoic rock beneath the PRU has much lower velocity (see discussion in text). The green boxes indicate areas of deformation on the lower Mesozoic section.

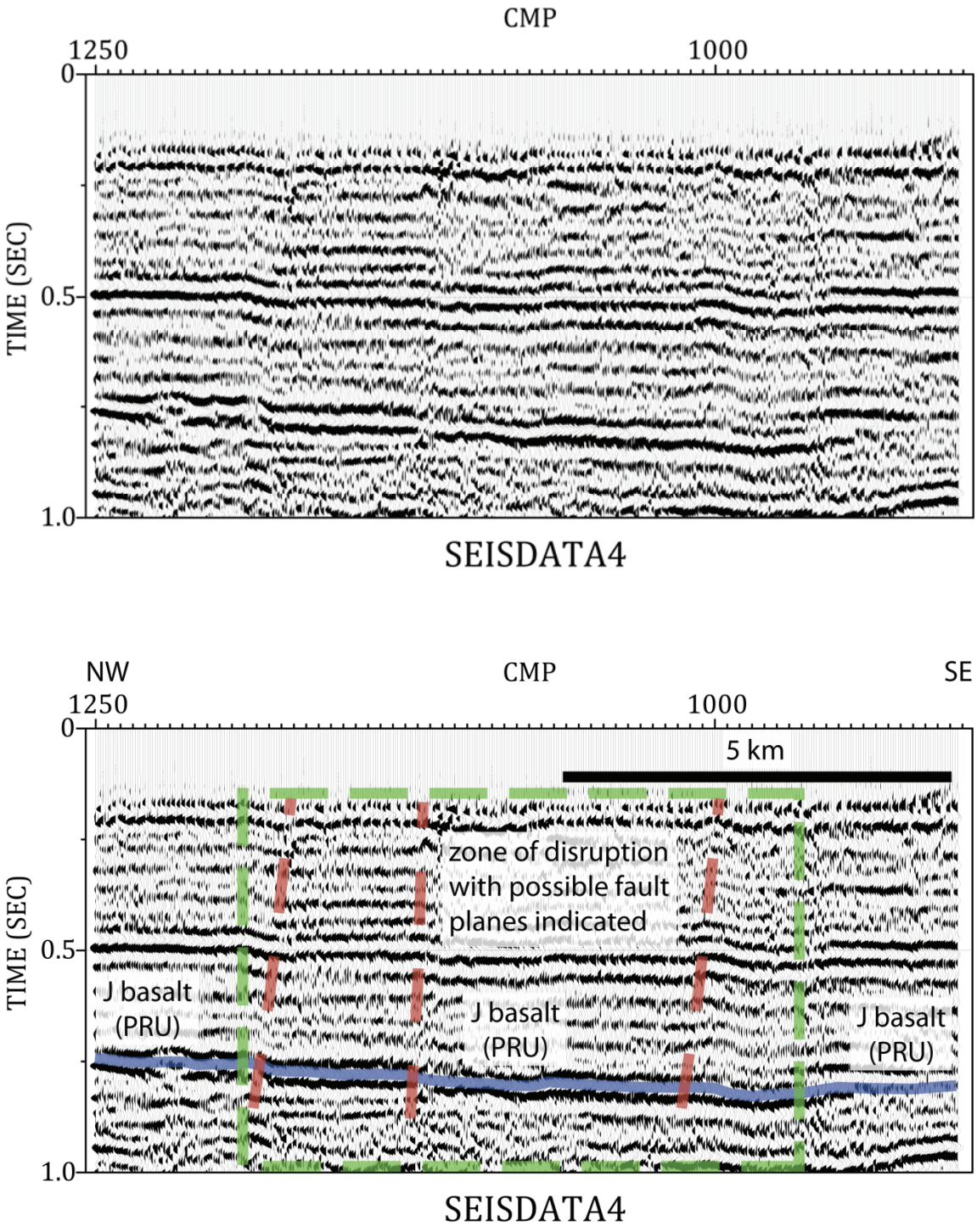

Figure 3.2: Reprocessed SEISDATA4 profile between CMP 900 to 1250, west of Rantowles, South Carolina. Refer to Figure 2.1 for location map. The dashed red lines indicate three interpreted faults affecting the coastal plain sediments. The contact between the Cretaceous and younger coastal plain sediments and the lower Mesozoic section (post-rift unconformity: PRU) is indicated by the blue line. In this section of the profile, the bright J reflection marks the PRU. The green box indicates areas of deformation on the lower Mesozoic section.

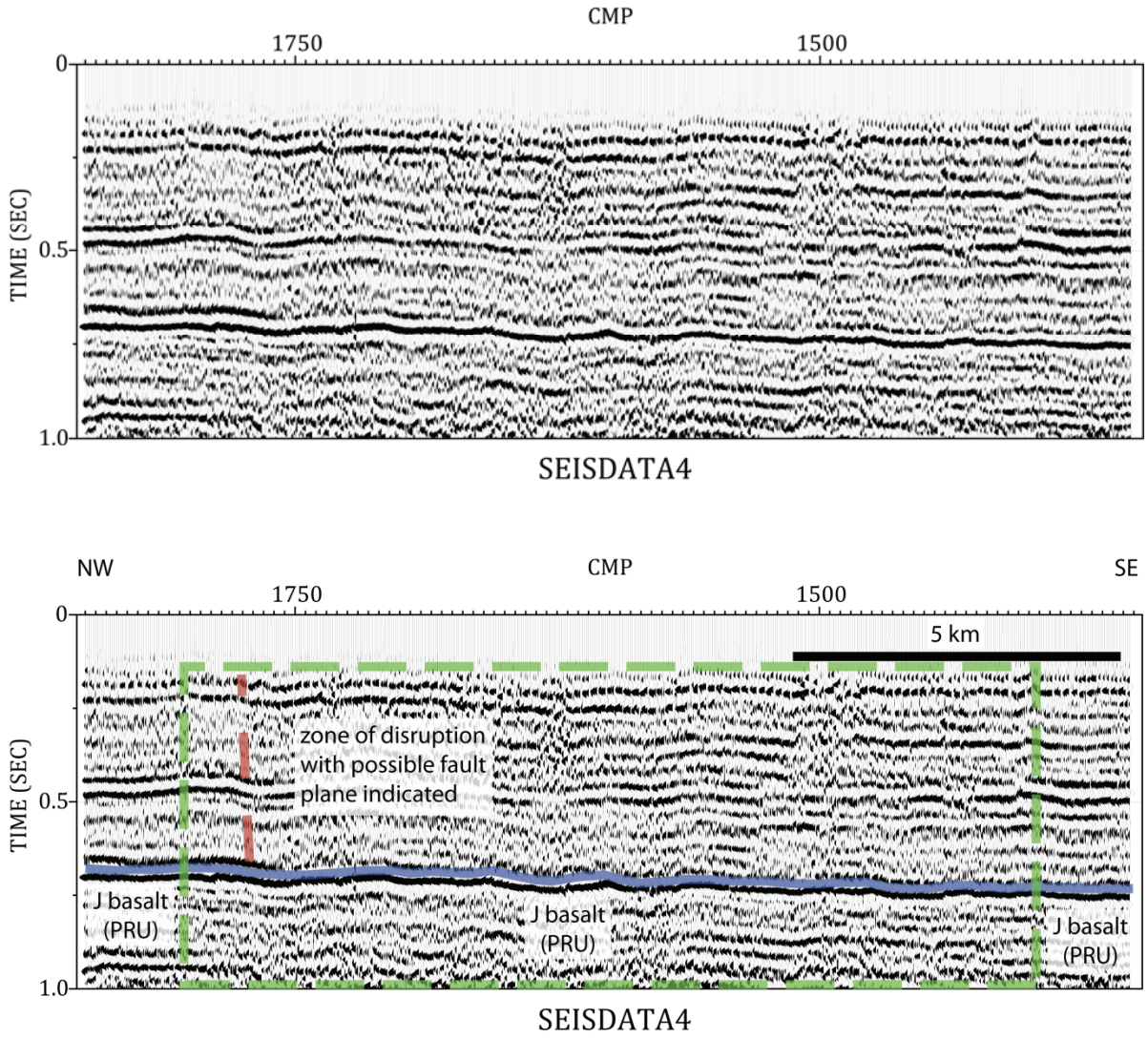

Figure 3.3: Reprocessed SEISDATA4 profile between CMP 1350 and 1850. This section trends north-south, parallel to the Edisto River. Refer to Figure 2.1 for location map. The dashed red lines indicate interpreted faults affecting the coastal plain sediments. This section of SEISDATA4 crosses the magnetic gradient, and deformation similar in style to that previously noted on other seismic profiles crossing the gradient in the study area is observed here as well. Note the zone of folding and general down-to-the-south deformation pattern. The contact between the Cretaceous and younger coastal plain sediments and the lower Mesozoic section (post-rift unconformity: PRU) is indicated by the blue line. It is marked by the bright reflection from the J basalt. The green box indicates deformation in the lower Mesozoic section.

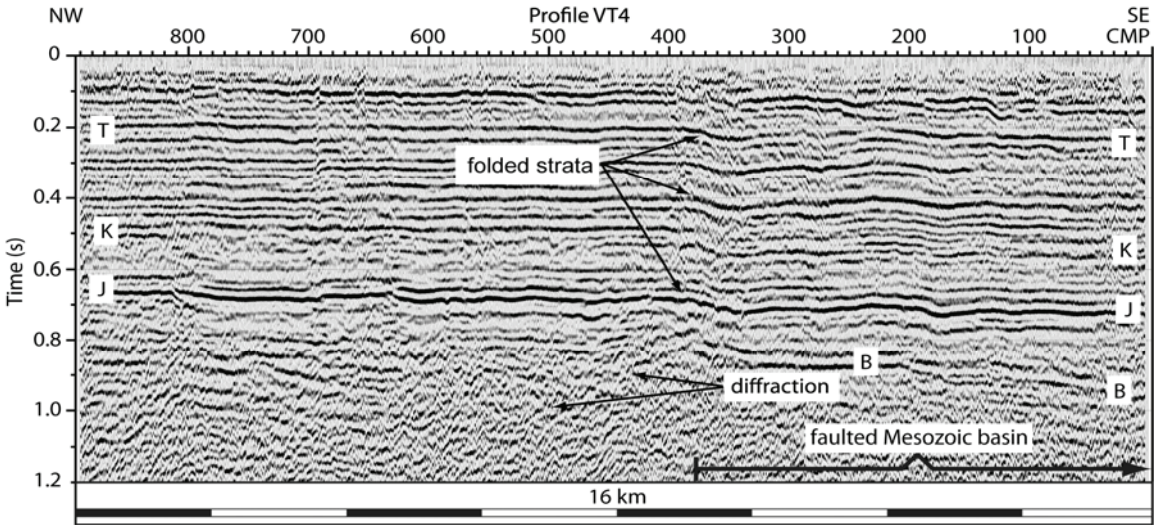

Figure 3.4: Profile VT-4. The profile is located to the west of Summerville (Figure 2.1) showing folding of Cenozoic sediments indicative of reactivation of Mesozoic faults in the vicinity of the magnetic gradient (see Figure 2.1 for location). Note that the B beds deepen to the southeast. This is interpreted to indicate young (Cenozoic) faulting at the northwestern margin of the basin structure defined by the B reflectors. Reflections labeled T and K are within the Tertiary-Cretaceous sediments. Reflection J is the top of the lower Mesozoic section. Used with permission of Seismological Society of America. From Chapman and Beale, On the Geologic Structure at the Epicenter of the 1886 Charleston, South Carolina, Earthquake, *Bull. Seismol. Soc Am.* **100**, 1010-1030, 2010, (c) Seismological Society of America.

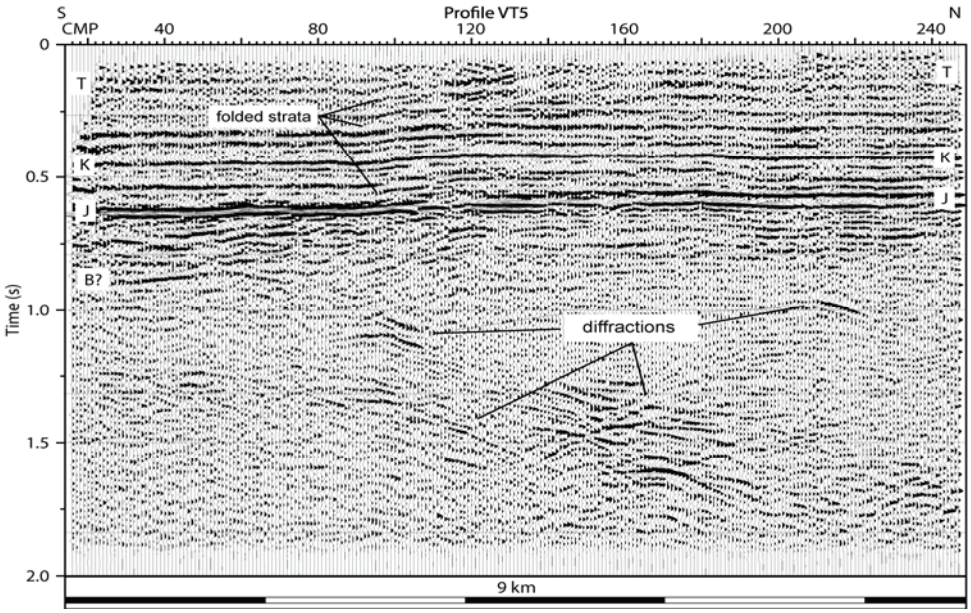

Figure 3.5: Monocline fold shown on profile VT-5. The fold is located along the magnetic gradient to the north of Summerville (Figure 2.1) is analogous to that observed on VT-4 (Figure 3.4) and on SEISDATA4 (Figure 3.3). Note that the beds on the south end of VT-5 are down-to-the-south, consistent with the sense of motion shown in both figures 3.3 and 3.4. Profiles VT4, VT5 and SEISDATA4 all indicate that the margin of the basin has been reactivated in a down-to-the-southeast sense in the Cenozoic. Used with permission of Seismological Society of America. From Chapman and Beale, On the Geologic Structure at the Epicenter of the 1886 Charleston, South Carolina, Earthquake, *Bull. Seismol. Soc Am.* **100**, 1010-1030, 2010, (c) Seismological Society of America.

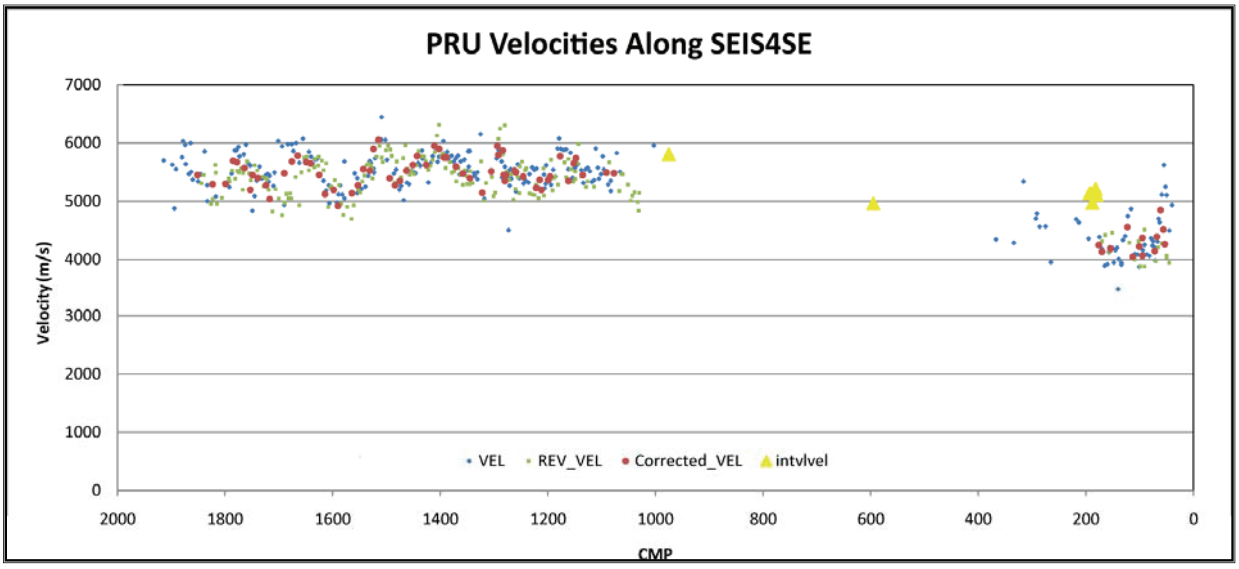

Figure 3.6: Refraction velocities on the top of the lower Mesozoic section along seismic profile SEISDATA4. Blue dots indicate velocity measurements in the up-dip direction. Green dots indicate velocity measurements in the down-dip direction. Red dots indicate corrected velocities based on up-dip and down-dip measurements. Yellow triangles indicate interval velocity measurements.

Chapter 4: Conclusions

The reprocessing of SEISDATA4 conducted in this study has resolved Cenozoic and Mesozoic faults to the south of Summerville and the Ashley River, where similar features had been discovered previously. The features imaged on SEISDATA4 indicate that the extensional basin that hosted the 1886 Charleston earthquake (and continues to host modern seismicity in the vicinity of Summerville) extends several kilometers to the south and west. In particular, faults of Cenozoic age are imaged at several locations along the profile, but are most clearly imaged along the section of the profile crossing the prominent magnetic gradient, in the vicinity of the Edisto River. Here, evidence of down-to-the southeast Cenozoic deformation of a style similar to that observed to the northeast nearer Summerville is clearly observed. The question as to which fault or faults slipped during the 1886 earthquake remains. Currently, seismicity is concentrated near Summerville, both along the western border of the imaged Mesozoic extensional feature, and within its interior. Similar features are currently aseismic along SEISDATA4.

The reprocessed SEISDAT4 profile images a change in the lithology of the Lower Mesozoic rocks immediately beneath the post-rift unconformity. The top of the Lower Mesozoic section along the northwestern half of the profile is comprised of an early Jurassic basalt flow, that is responsible for the very prominent “J” reflection apparent on other reflection profiles in the study area. That feature appears to terminate near the middle of the SEISDATA4 profile in the vicinity of CMP 1000. This was inferred by previous investigators on the basis of another reflection profile that was co-located with SEISDATA4 (Hamilton et al., 1983). This refraction analysis confirms that earlier inference, and provides better resolution of the Lower Mesozoic section. The termination of the strong J reflection occurs in a section of the profile that shows

major disruption of the underlying B reflections, and suggests that the termination of the basalt flow responsible for the J reflection may be related to tectonic deformation.

References

Bakun, W. H., and M. G. Hopper (2004). Magnitudes and locations of the 1811–1812 New Madrid Missouri and the 1886 Charleston, South Carolina, earthquake, *Bull. Seismol. Soc. Am.* **94,** 64-75

Behrendt, J. C. (1986). Structural interpretation of multichannel seismic reflection profiles crossing the southeastern United States and the adjacent continental margin—Décollement, faults, Triassic(?) basins and Moho reflections, in *Reflection Seismology: The Continental Crust*, M. Barazangi and L. Brown (Editors), American Geophysical Union Geodynamics Series, **14**, 201-214.

Carmichael, R. S. (1982). *CRC Handbook of Physical Properties of Rocks*, Vol. **II**, CRC Press, Inc., Boca Raton, Florida, 345 p.

Chapman, M.C., and J.N. Beale (2008). Mesozoic and Cenozoic faulting imaged at the epicenter of the 1886 Charleston, South Carolina, earthquake, *Bull. Seismol. Soc. Am.* **98,** 2533-2542

Chapman, M. C., J. N. Beale, and R. D. Catchings (2008). *Q* for *P*-waves in the sediments of the Virginia Coastal Plain, *Bull. Seismol. Soc. Am.* **98,** 2022-2032.

Chapman, M.C., and J.N. Beale (2010). On the Geologic Structure at the Epicenter of the 1886 Charleston, South Carolina, Earthquake, *Bull. Seismol. Soc Am.* **100**, 1010-1030

Chowns, T.M. and C.T. Williams (1983). Pre-Cretaceous rocks beneath the Georgia Coastal Plain – regional implications, *in* Gohn, G.S., ed., Studies Related to the Charleston, South Carolina, Earthquake of 1886--Tectonics and Seismicity, *U.S. Geological Survey Professional Paper 1313*, L1-L42.

Daniels, D.L., I. Zietz and P. Popenoe (1983). Distribution of subsurface lower Mesozoic rocks in the Southeastern United States as interpreted from regional aeromagnetic and gravity maps, *in* Gohn, G.S., ed., Studies Related to the Charleston, South Carolina, Earthquake of 1886--Tectonics and Seismicity, *U.S. Geological Survey Professional Paper 1313*, K1-K24.

Daniels, D. L. (2005). South Carolina aeromagnetic and gravity maps and data: A website for distribution of data, U.S. Geol. Surv. Open File Rept. 2005-1022: available at http://pubs.usgs.gov/of/2005/1022/ (last accessed August 2009).

Dutton, C (1889). The Charleston earthquake of August 31, 1886, in Ninth Annual Report of the U.S. Geological Survey, 203-528

Gohn, G.S., B.H. Higgins, C.C. Smith and J.P. Owens (1977). Lithostratigraphy of the deep corehole (Clubhouse Crossroads corehole 1) near Charleston, South Carolina, *in* Rankin, D.W., ed., Studies Related to the Charleston, South Carolina Earthquake of 1886 - A Preliminary Report, *U.S. Geol. Survey Professional Paper 1028*, 59-69.

Gohn, G.S. (1983a). Editor's Preface *to* Studies Related to the Charleston, South Carolina Earthquake of 1886-- Tectonics and Seismicity, *U.S. Geological Survey Professional Paper 1313*, vii.

Gohn, G.S. (1983b). Geology of the basement rocks near Charleston, South Carolina - Data from detrital rock fragments in Lower Mesozoic(?) rocks in Clubhouse Crossroads test hole #3, *in* Gohn, G.S., ed., Studies Related to the Charleston, South Carolina, Earthquake of 1886--Tectonics and Seismicity, *U.S. Geological Survey Professional Paper 1313*, E1-E22.

Hamilton, R.M., J.C. Behrendt, and H.D. Ackermann (1983). Land multichannel seismic-reflection evidence for tectonic features near Charleston, South Carolina, *in* Gohn, G.S., ed., Studies

Related to the Charleston, South Carolina, Earthquake of 1886--Tectonics and Seismicity, *U.S. Geological Survey Professional Paper 1313*, I1-I18.

Johnston, A. C. (1996). Seismic moment assessment of earthquakes in stable continental regions—III. New Madrid 1811–1812, Charleston 1886 and Lisbon 1755, *Geophys. J. Int.* **126,** 314-344

Lanphere, M.A. (1983). 40Ar/39Ar ages of basalt from Clubhouse Crossroads test hole #2, near Charleston, South Carolina, *in* Gohn, G.S., ed., Studies Related to the Charleston, South Carolina, Earthquake of 1886--Tectonics and Seismicity, *U.S. Geological Survey Professional Paper 1313*, B1-B8.

Luetgert, J. H., H. M. Benz, and S. Madabhushi (1994). Crustal structure beneath the Atlantic Coastal Plain of South Carolina, *Seism. Res. Lett.* **65,** 180-191

McBride, J.H., K.D. Nelson and L.D. Brown (1989). Evidence and implications of an extensive early Mesozoic rift basin and basalt/diabase sequence beneath the southeast Coastal Plain, *Bull. Geol. Soc. Am*.,101, 512-520.

McBride, J.H. (1991). Constraints on the structure and tectonic development of the early Mesozoic South Georgia Rift, southeastern United States; seismic reflection data processing and interpretation, *Tectonics*, 10, no. 5, 1065-1083.

Petersen, M. D., A. D. Frankel, S. C. Harmsen, C. S. Mueller, K. M. Haller, R. L. Wheeler, R. L. Wesson, Y. Zeng, O. S. Boyd, D. M. Perkins, N. Luco, E. H. Field, C. J. Wills, and K. S. Rukstales (2008). Documentation for the 2008 update of the United States National Seismic Hazard Maps, U.S. Geol. Surv. Open File Rept. 2008-1128, 60 pp.

Rankin, D. W. (1977). Studies related to the Charleston, South Carolina, earthquake of 1886—A preliminary report, U.S. Geol. Surv. Profess. Pap. 1028, 204 pp.

Reid, M.S., W.R. Aucott, R.W. Lee and R.A. Renken (1986). Hydrologic and geologic analysis of a well in Dorchester County, South Carolina, *U.S. Geological Survey Water-Resources Investigations Report 86-4161*.

Talwani, P., and W. T. Schaeffer (2001). Recurrence rates of large earthquakes in the South Carolina Coastal Plain based on paleoliquefaction data, *J. Geophys. Res.* **106,** no. B4, 6621-6642

Telford, W.M, L.P. Geldart, R.E. Sheriff (1990). *Applied Geophyisics*, Cambridge University Press, Cambridge, UK, 770 p.

Thomas, W.A. T.M. Chowns, D.L.Daniels, T.L. Neathery, L. Glover and R.J. Geason (1989). *The subsurface Appalachians-Ouachita Orogen in the United States*, R.D. Hatcher, Jr., W.A. Thomas and G.W. Viele, ed., Geological Society of America, Boulder, CO.

Yilmaz, O. 1987. Seismic Data Processing: Society of Exploration Geophysicists, Tulsa, Oklahoma. 526 p.

Appendix A: Full Stacked CMP Sections of SEISDATA4

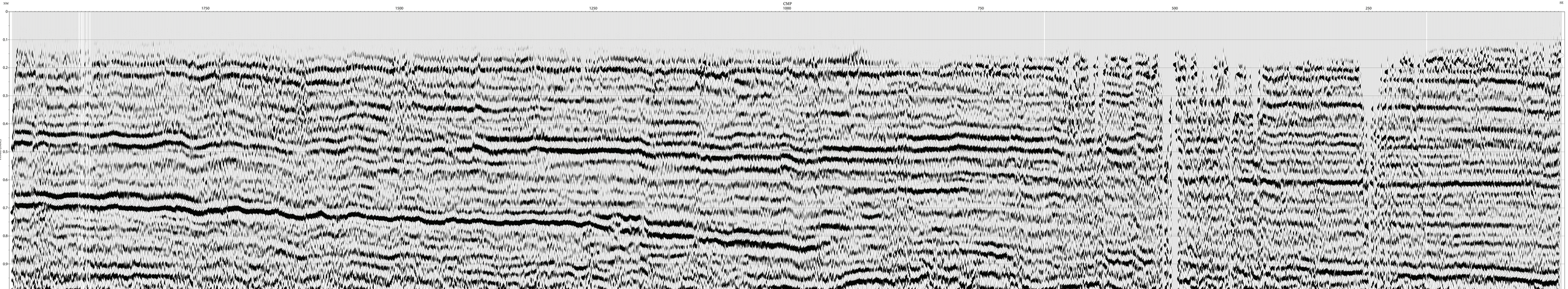

Figure A.1: CMP stacked section of SEISDATA4 from 0 to 1 seconds two-way travel time. Only near offsets of less than 1 km were considered for this stacked section.

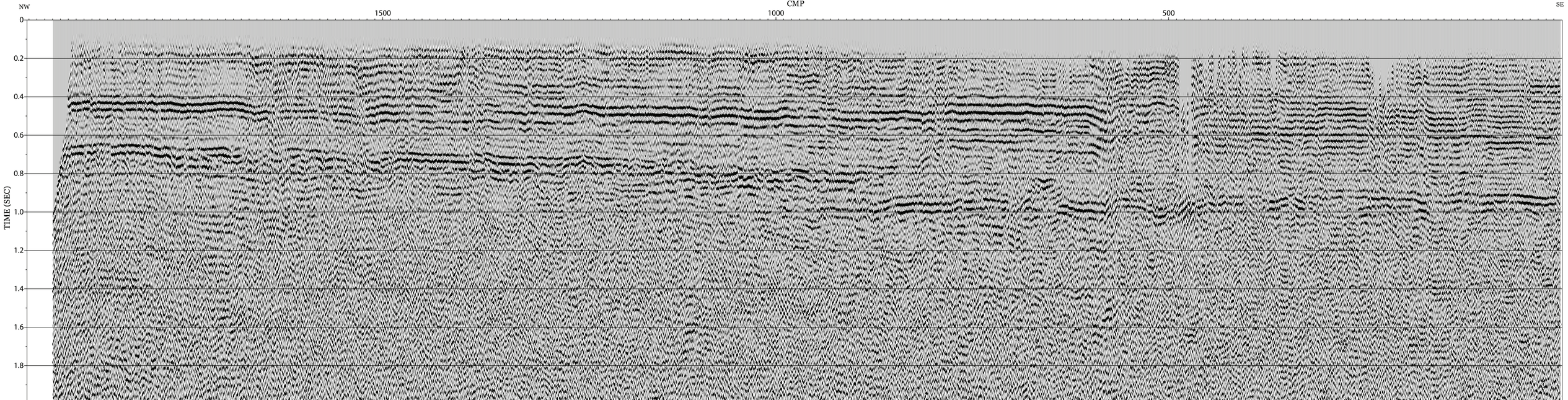

Figure A.2: CMP stacked section of SEIDATA4 from 0 to 2 seconds two-way travel time. For this stack all offsets were considered.